

Mn-rich MnSb_2Te_4 : A topological insulator with magnetic gap closing at high Curie temperatures of 45–50 K

S. Wimmer^{1,+}, J. Sánchez-Barriga^{2,+}, P. Küppers^{3,+}, A. Ney¹, E. Schierle², F. Freyse^{2,4}, O. Caha⁵, J. Michalička⁶, M. Liebmann³, D. Primetzhofer⁷, M. Hoffmann⁸, A. Ernst^{8,9}, M. M. Otrokov^{10,11}, G. Bihlmayer¹², E. Weschke², B. Lake², E. V. Chulkov^{13,14,15,16}, M. Morgenstern³, G. Bauer¹, G. Springholz^{1*}, O. Rader^{2*}

¹*Institut für Halbleiter- und Festkörperphysik,*

Johannes Kepler Universität, Altenberger Straße 69, 4040 Linz, Austria

²*Helmholtz-Zentrum Berlin für Materialien und Energie,*

Albert-Einstein-Straße 15, 12489 Berlin, Germany

³*II. Institute of Physics B and JARA-FIT,*

RWTH Aachen University, 52074 Aachen, Germany

⁴*Institut für Physik und Astronomie, Universität Potsdam,*

Karl-Liebknecht-Straße 24/25, 14476 Potsdam, Germany

⁵*Department of Condensed Matter Physics, Masaryk University,*

Kotlářská 267/2, 61137 Brno, Czech Republic

⁶*Central European Institute of Technology, Brno University of Technology,*

Purkyňova 123, 612 00 Brno, Czech Republic

⁷*Department of Physics and Astronomy, Universitet Uppsala,*

Lägerhyddsvägen 1, 75120 Uppsala, Sweden

⁸*Institute for Theoretical Physics, Johannes Kepler Universität,*

Altenberger Straße 69, 4040 Linz, Austria

⁹*Max Planck Institute of Microstructure Physics,*

Weinberg 2, 06120 Halle, Germany

¹⁰*Centro de Física de Materiales (CFM-MPC),*

Centro Mixto CSIC-UPV/EHU, 20018 San Sebastián/Donostia, Spain

¹¹*IKERBASQUE, Basque Foundation for Science, 48011 Bilbao, Spain*

¹²*Peter Grünberg Institute and Institute for Advanced Simulation,*

Forschungszentrum Jülich and JARA, 52425 Jülich, Germany

¹³*Donostia International Physics Center (DIPC),*

20018 San Sebastián/Donostia, Spain

¹⁴*Departamento de Física de Materiales,*

Facultad de Ciencias Químicas, Universidad del País Vasco,

Apdo. 1072, 20080 San Sebastián/Donostia, Spain

¹⁵*Saint Petersburg State University,*

198504, Saint Petersburg, Russia and

¹⁶*Tomsk State University, Tomsk, 634050, Russia*

(Dated: April 27, 2021)

Abstract

Ferromagnetic topological insulators exhibit the quantum anomalous Hall effect that might be used for high precision metrology and edge channel spintronics. In conjunction with superconductors, they could host chiral Majorana zero modes which are among the contenders for the realization of topological qubits. Recently, it was discovered that the stable $2+$ state of Mn enables the formation of intrinsic magnetic topological insulators with $A_1B_2C_4$ stoichiometry. However, the first representative, $MnBi_2Te_4$, is antiferromagnetic with 25 K Néel temperature and strongly n-doped. Here, we show that p-type $MnSb_2Te_4$, previously considered topologically trivial, is a ferromagnetic topological insulator in the case of a few percent of Mn excess. It shows (i) a ferromagnetic hysteresis with record high Curie temperature of 45–50 K, (ii) out-of-plane magnetic anisotropy and (iii) a two-dimensional Dirac cone with the Dirac point close to the Fermi level which features (iv) out-of-plane spin polarization as revealed by photoelectron spectroscopy and (v) a magnetically induced band gap that closes at the Curie temperature as demonstrated by scanning tunneling spectroscopy. Moreover, it displays (vi) a critical exponent of magnetization $\beta \sim 1$, indicating the vicinity of a quantum critical point. *Ab initio* band structure calculations reveal that the slight excess of Mn that substitutionally replaces Sb atoms provides the ferromagnetic interlayer coupling. Remaining deviations from the ferromagnetic order, likely related to this substitution, open the inverted bulk band gap and render $MnSb_2Te_4$ a robust topological insulator and new benchmark for magnetic topological insulators.

Corresponding authors: O. Rader, email: rader@helmholtz-berlin.de, G. Springholz, email: gunther.springholz@jku.at.

+ These authors contributed equally to the present work.

The quantum anomalous Hall effect (QAHE) offers quantized conductance and lossless transport without the need for an external magnetic field [1]. The idea to combine ferromagnetism with topological insulators for this purpose [2–4] has fuelled the materials science [5]. It led to the experimental discovery of the QAHE in Cr- and V- doped $(\text{Bi}, \text{Sb})_2\text{Te}_3$ [6–10] with precise quantized values of the Hall resistivity down to the sub-part-per-million level [11–14]. The stable 3+ configuration of V or Cr substitutes the isoelectronic Bi or Sb [3, 15, 16] enabling ferromagnetism by coupling the magnetic moments of the transition metal atoms. Hence, time-reversal symmetry is broken enabling, through perpendicular magnetization, a gap opening at the Dirac point of the topological surface state [2–5]. This gap hosts chiral edge states with precisely quantized conductivity. However, the experimental temperatures featuring the QAHE are between 30 mK [6, 12] and a few K [17, 18] only, significantly lower than the ferromagnetic transition temperatures T_C in these systems [19]. If the temperature of the QAHE could be raised, applications such as chiral interconnects [20], edge state spintronics [21, 22] and metrological standards [13, 14] become realistic.

One promising approach is the so-called modulation doping in which the magnetic dopants are located only in certain parts of the topological insulator. This implies strong coupling of the topological surface state to the magnetic moments at a reduced disorder level [17, 23]. Most elegantly, this has been realized for Mn doped Bi_2Te_3 and Bi_2Se_3 . The tendency of Mn to substitute Bi is weak, such that Mn doping leads to the spontaneous formation of septuple layers with MnBi_2Te_4 stoichiometry. These septuple layers are statistically distributed among quintuple layers of pure Bi_2Te_3 or Bi_2Se_3 at low Mn concentration [24, 25] and increase in number with increasing Mn concentration [24]. Eventually, only septuple layers remain when the overall stoichiometry of MnBi_2Te_4 or MnBi_2Se_4 [25, 26] is reached. Density functional theory (DFT) calculations found that MnBi_2Te_4 forms ferromagnetic layers with antiferromagnetic interlayer coupling [27, 28] as confirmed by experiments at low temperatures [28–31]. As a result, MnBi_2Te_4 is an *antiferromagnetic* topological insulator [28, 32–35] that can exhibit axion states [5]. The QAHE, however, has only been realized in a limited way: ultra thin flakes consisting of odd numbers of septuple layers exhibited an anomalous Hall effect (AHE) that is nearly quantized. This is caused by the uncompensated ferromagnetic septuple layer without partner. Nevertheless, exact quantization still required a magnetic field [36]. A ferromagnetic AHE has also been observed for systems with either a larger amount of quintuple layers [37–39] or via alloying of Sb and Bi in $\text{Mn}(\text{Bi}_{2-x}\text{Sb}_x)_2\text{Te}_4$

[30, 31, 40] or both [41, 42]. Most notably, a nearly quantized AHE has been observed up to 7 K for a $\text{MnBi}_2\text{Te}_4/\text{Bi}_2\text{Te}_3$ heterostructure after unconventional counter doping inducing vacancies by electron bombardment [18].

A central drawback of the Bi_2Te_3 and Bi_2Se_3 host materials is their strong n-type doping. In contrast, Sb_2Te_3 is p-doped and much closer to charge neutrality [43]. Indeed, mixtures of Bi_2Te_3 and Sb_2Te_3 with stoichiometries close to Sb_2Te_3 have been employed for the QAHE using Cr and V doping [6–10]. Magnetism of dilute Mn-doped Sb_2Te_3 has initially been studied by Dyck *et al.* obtaining $T_C \simeq 2\text{ K}$ and perpendicular anisotropy [44]. Later, a higher $T_C = 17\text{ K}$ was reported for 1.5% Mn-doping [45]. Stoichiometric bulk MnSb_2Te_4 provided both antiferromagnetism (Néel temperature $T_N = 20\text{ K}$) [30, 31, 46] and ferromagnetism ($T_C = 25 - 34\text{ K}$) [46–48] depending on the synthesis conditions. By comparison with scattering methods, it has been conjectured that this is related to a remaining Mn-Sb exchange within the septuple layers [41, 46, 49, 50] that could even lead to spin glass behaviour [50]. DFT calculations, found that the perfectly ordered MnSb_2Te_4 is antiferromagnetic [27], but topologically trivial [51–55], while Mn-Sb exchange can render the interlayer coupling ferromagnetic [46, 49].

Here, epitaxial MnSb_2Te_4 is studied using spin- and angle-resolved photoemission spectroscopy (ARPES), scanning tunneling microscopy (STM) and spectroscopy (STS), magnetometry, x-ray magnetic circular dichroism (XMCD) and DFT. All experimental methods were performed as a function of temperature to pin down the intricate correlation between magnetism and non-trivial band topology essential for the QAHE. It is revealed that the material unites the favorable properties of a topological insulator with its Dirac point close to the Fermi level E_F with that of a ferromagnetic hysteresis with out-of-plane anisotropy and record-high T_C , twice as high as the T_N previously reported for antiferromagnetic MnBi_2Te_4 and MnSb_2Te_4 [30, 31]. Moreover, temperature dependent STS finds a magnetic gap of 17 meV at E_F for 4.3 K that closes rather exactly at T_C as expected for a ferromagnetic topological insulator. By combining DFT, STM, Rutherford backscattering (RBS), and x-ray diffraction (XRD) it is uncovered that a partial substitution of Sb atoms by Mn is decisive to render MnSb_2Te_4 both ferromagnetic *and* topologically non-trivial.

Epitaxial MnSb_2Te_4 films with 200 nm thickness were grown by molecular beam epitaxy (MBE) (Supplementary Section I). Figure 1a shows the cross section of the MnSb_2Te_4 lattice structure revealed by high resolution scanning transmission electron microscopy (TEM). It

consists of septuple layers (SL) with stacking sequence Te-Sb-Te-Mn-Te-Sb-Te, Figure 1c. This corresponds to the MnSb_2Te_4 stoichiometry as verified by Rutherford backscattering spectrometry (RBS), however, with a minor excess of Mn (7%) compensating a minor deficiency of Sb (Supplement: Figure 5). Like with $\text{MnBi}_2\text{Te}_4/\text{Bi}_2\text{Te}_3$ [56], the exchange coupling is strongly enhanced in these septuple layers relative to a system where Mn substitutes Bi randomly. (24–25 K) [30, 31].

The nearly exclusive formation of septuple layers in the entire MnSb_2Te_4 samples is confirmed by high-resolution XRD (Supplement: Figure 6), revealing only a minute number of residual quintuple layers. In contrast, TEM and XRD analysis of V-doped $(\text{Bi}, \text{Sb})_2\text{Te}_3$ shows quintuple layers only [57]. This highlights that septuple layers are unfavorable for V^{3+} . They require the addition of a charge neutral transition metal $^{2+}/\text{Te}^{2-}$ bilayer to each quintuple layer as easily possible for Mn^{2+} but not for V^{3+} . Detailed XRD analysis again points to an exchange of Mn and Sb within the septuple layers in the 10% range (Supplement: Figure 6). This implies that Mn does not reside exclusively in the center of the septuples, but also to a small extent on Sb sites in the adjacent lattice planes. Indeed, STM images of the atomically flat and Te terminated surface of MnSb_2Te_4 epilayers (Figure 1b) exhibit triangular features, pointing to defects in the cation layer beneath the surface [58, 59]. These defects occur with an atomic density of 5 – 10%. Since this is significantly larger than in undoped Sb_2Te_3 films [58], the triangles are most likely caused by subsurface Mn atoms on Sb sites, in line with the XRD and RBS results. As shown by DFT below, these defects turn out to be decisive for the ferromagnetic interlayer coupling in MnSb_2Te_4 . Similar conjectures based on scattering methods have been raised previously [41, 46, 49, 50] as well as for MnBi_2Te_4 based on STM results [60].

Figure 1d displays the temperature dependent magnetization $M(T)$ measured by a superconducting quantum interference device (SQUID). The measurements were recorded at 10 mT after magnetizing the sample at 2 K by a magnetic field of 5 T perpendicular (blue) or parallel (red) to the film surface. Most strikingly, all MnSb_2Te_4 epilayers show pronounced *ferromagnetic* behavior by $M(H)$ hysteresis loops (Figure 1e). A record high T_C of 45, 46–48 and 50 K is revealed for three independent samples (Supplement: Figure 7), significantly larger as the antiferromagnetic and ferromagnetic transition temperatures of bulk crystals (Supplement: Table I), and twice as large as the $T_N \leq 25$ K obtained for MnBi_2Te_4 films grown under nearly identical conditions. It has been crosschecked that the displayed

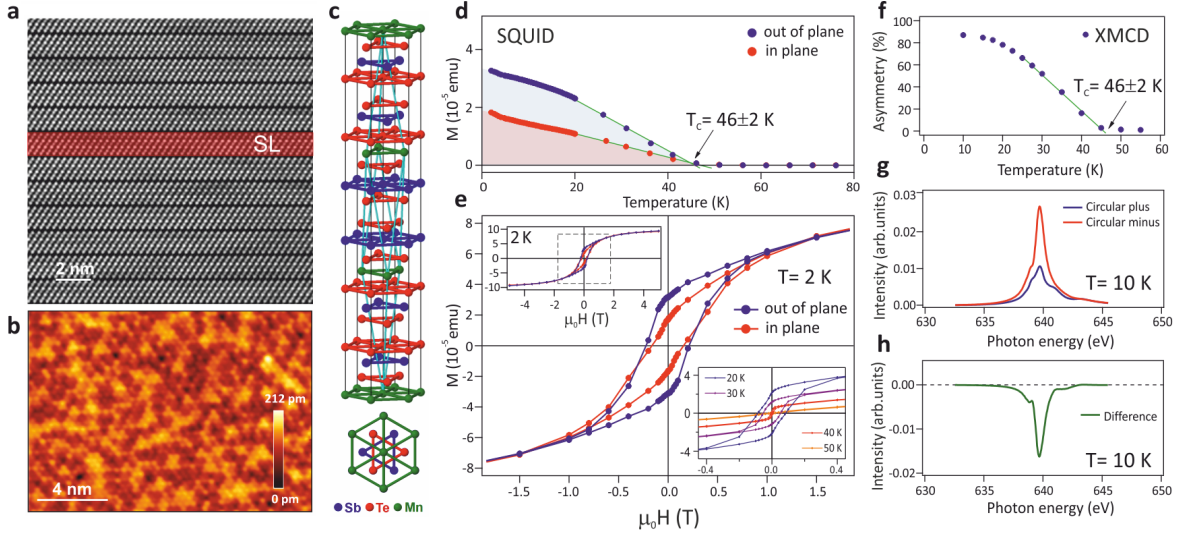


FIG. 1: **Structural and magnetic properties of epitaxial MnSb_2Te_4 .** (a) Cross-sectional scanning TEM image of the septuple layer sequence formed in the MnSb_2Te_4 films on BaF_2 substrates. For clarity, one of the septuples is highlighted by red color and denoted as SL. The weak van-der-Waals-like bond between the Te-terminated septuple layers is the natural surface termination. (b) STM image of the flat topography of this surface, recorded at $T = 4.3$ K, sample voltage of 500 mV and current of 200 pA. (c) Sketch of the ideal crystal structure as side view and top view. (d) SQUID magnetometry as a function of temperature recorded at 10 mT after field cooling at 5 T. (e) Hysteresis loops probed by SQUID. The inset shows a larger H range. Perpendicular anisotropy can be deduced from the larger out-of-plane signal. (f) Temperature dependent XMCD signal at the Mn L_3 -edge and the (0001) Bragg peak position recorded in x-ray scattering geometry at 0 T after field cooling in 0.5 T. (g) Corresponding full XMCD spectra recorded with opposite circular polarizations at 10 K. (h) Difference of the spectra in (g). Linear extrapolation in (d,f) (green lines) reveals a ferromagnetic Curie temperature $T_C = 46 \pm 2$ K for both experimental probes.

remanent magnetization is exactly the same as in the corresponding hysteresis loops.

In particular, the large remanent magnetization observed by the bulk sensitive SQUID measurements excludes that it is caused by uncompensated antiferromagnetic septuple layers only [36]. The $M(H)$ hysteresis curve (Figure 1e), however, shows a rounded shape that persists up to fields much higher than those typical for domain reversals and does not saturate up to ± 5 T where the magnetic moment per Mn atom is still less than $2 \mu_B$, similar

to the result for antiferromagnetic MnSb_2Te_4 [30]. Recently, it was found that 60 T are required to fully polarize a MnSb_2Te_4 bulk-type sample [61]. This suggests additional types of competing magnetic orders. Indeed, a kink in $M(T)$ is observed at 20–25 K (Supplement: Figure 7), close to the Néel temperature reported earlier for MnSb_2Te_4 [30]. This implies that the high-temperature ferromagnetism is most likely accompanied by ferrimagnetism as also supported by the relatively large in-plane hysteresis and magnetization, Figure 1e, in line with observations of competing ferro- and antiferromagnetic order in bulk MnSb_2Te_4 [39, 41, 46, 48–50, 61].

The ferromagnetism is confirmed by element specific, *zero field* XMCD recorded in diffraction geometry. For these measurements, the sample was remanently magnetized at ~ 0.5 T and 10 K. From spectra recorded with oppositely circularly polarized light at the (0001) Bragg peak, the intensity difference $C_+ - C_-$ (Figure 1h) was deduced for 0 T with the photon energy tuned to the Mn- L_3 resonance (Figure 1g). The asymmetry $(C_+ - C_-)/(C_+ + C_-)$ directly yields the magnetization of the Mn. Its temperature dependence (Figure 1f) impressively confirms the SQUID data with high $T_C \simeq 46$ K and unambiguously attributes the ferromagnetism to the Mn atoms. The record-high T_C with magnetic easy axis perpendicular to the surface (crystallographic c -axis) as well as the large coercivity (~ 0.2 T), (~ 10 mT at 5 K) [47] and $\text{MnSb}_{1.88}\text{Bi}_{0.02}\text{Te}_4$ single crystals (31 mT at 2 K) [31] Shi2020 findet auch 0.2 T. renders the samples very robust ferromagnets.

Note that the spin-orbit interaction is crucial for both out-of-plane easy axis and large coercivity [24]. While it is sufficiently strong to turn the magnetization out of plane in Mn-containing Bi_2Te_3 , the atomic weight of Se in MnBi_2Se_4 is too weak [24, 62]. The present data reveals that Sb_2Te_3 is sufficiently heavy, i.e., spin-orbit coupling sufficiently large, to maintain the perpendicular anisotropy for high Mn content.

To elucidate the origin of the ferromagnetism, DFT calculations are employed (Supplement: Table III). They firstly highlight the differences between MnSb_2Te_4 and MnBi_2Te_4 . In both cases, the in-plane Mn coupling within each septuple layer is ferromagnetic. It is unlikely that the observed difference between antiferromagnetic interlayer coupling in MnBi_2Te_4 and ferromagnetic interlayer coupling in epitaxial MnSb_2Te_4 is caused by the lowered spin-orbit interaction, since it remained large enough for out-of-plane anisotropy. However, the in-plane lattice constant a is by $\sim 2\%$ smaller for MnSb_2Te_4 . Hence, the DFT based exchange constants of MnSb_2Te_4 for the in-plane lattice constant a determined by

XRD and for a expanded to the value of MnBi_2Te_4 are compared (Supplement: Table III). While the in-plane compression increased the in-plane exchange constant J between nearest neighbors by almost a factor of three, T_N is barely changed. The reason is that the enlarged in-plane overlap of Mn d states weakens the already small, perpendicular interlayer coupling. Consequently, the energy gain of antiferromagnetism against ferromagnetism becomes as low as 0.6 meV per Mn atom. This suggests that small structural changes along the interlayer exchange path can induce the transition to ferromagnetic order.

The XRD and RBS data imply a Mn-Sb site exchange. One possibility is to exchange the Mn from the central layer with Sb from the adjacent cation layers. Here, DFT calculations demonstrate that already 2.5% of Mn on the Sb sites, respectively, 5% of Mn replacement by Sb in the central layer, is sufficient to swap the sign of the interlayer exchange constant (Supplement: Table III). This renders MnSb_2Te_4 ferromagnetic at a site exchange that agrees well with both the XRD analysis and the density of subsurface defects observed by STM (Figure 1b). A similar site exchange was recently observed for single crystals of bulk MnSb_2Te_4 [46, 47, 50] and $\text{MnSb}_{1.88}\text{Bi}_{0.02}\text{Te}_4$ [31]. This corroborates that the Mn-Sb site exchange is easily enabled. Thus, it is conjectured that MnSb_2Te_4 single crystals remain antiferromagnetic [31] only for negligible Sb-Mn intermixing. However, the modelled Mn-Sb site exchange barely increases the transition temperature ($T_N = 18\text{ K} \rightarrow T_C = 25\text{ K}$ (Supplement: Table III). Instead, 5% excess Mn incorporated substitutionally in the Sb layers without removing it from the central layer leads to $T_C = 44\text{ K}$ (Supplement: Table III) reproducing the experimental $T_C = 45 - 50\text{ K}$. Such T_C enhancement is caused by strengthening both the intra- and interlayer exchange constants simultaneously. The conclusion is robust towards charge doping by up to 0.2% Te or Sb vacancies that negligibly changes T_C (Supplementary Section XI). Note that the excess Mn in the Sb layer without Sb in the Mn layer and the resulting Sb deficiency nicely match the RBS results (Supplement: Figure 5)

Next, the topological properties of the epitaxial MnSb_2Te_4 are probed recalling that purely stoichiometric MnSb_2Te_4 was predicted to be topologically trivial [51–54]. It becomes a topological insulator only by replacement of more than half of the Sb by Bi [52] or by compressing the lattice by 3% [51]. However, the ARPES data from the MnSb_2Te_4 epilayers reveal the existence of a surface state with the dispersion of a Dirac cone along the wave vector parallel to the surface \mathbf{k}_{\parallel} (Figure 2a,c,d,f,h). Varying the photon energy (Figure 2a,b,

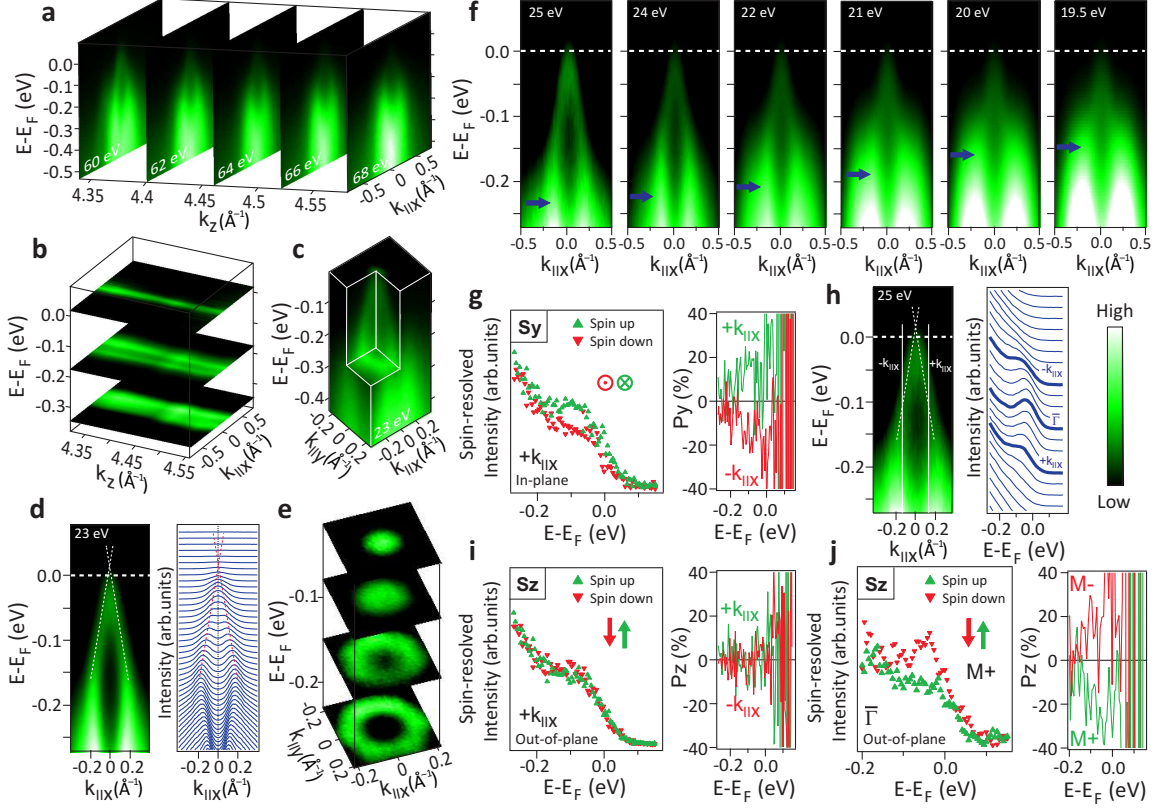


FIG. 2: **Topological properties of MnSb_2Te_4 revealed by ARPES.** (a) ARPES maps along $E(k_{\parallel x})$ for five different photon energies $h\nu$ displayed at the deduced k_z values. (b) Same data as (a) displayed as $(k_{\parallel x}, k_z)$ maps via interpolation featuring negligible dispersion along k_z . The k_z range covers the whole Brillouin zone. (c) Full 3D representation of the surface Dirac cone with $k_{\parallel x}$ pointing along the $\bar{\Gamma}\text{-}\bar{K}$ direction. (d) Energy-momentum dispersion of the Dirac cone (left) and corresponding momentum-distribution curves (right) recorded at $h\nu=23$ eV. Dashed, red lines along maxima result from fits to the data (Supplementary Section VIII). They extrapolate to a Dirac point 20 meV above the Fermi level. (e) Constant-energy cuts of the Dirac cone. (f) ARPES maps along $E(k_{\parallel x})$ at different photon energies featuring a strong dispersion of a bulk valence band (blue arrows) with photon energy (i.e., k_z). (g,i) Spin-resolved ARPES at k_{\parallel} as marked in (h), hence, crossing the surface Dirac cone. Left: spectra for the two spin channels at one $k_{\parallel,x}$. Right: spin polarization for both $k_{\parallel,x}$, i.e., $\pm k_{\parallel,x}$. (g) In-plane spin direction S_y perpendicular to k_{\parallel} . (i) Out-of-plane spin direction S_z . Data for S_x in Supplement: Figure 8. (h) Left: surface Dirac cone with marked k_{\parallel} of the spectra in (g,i) and dashed line along intensity maxima as deduced by fitting (Supplementary Section VIII). Right: energy distribution curves showing where g,i,j were measured. (j) Spin polarized ARPES recorded at $\bar{\Gamma}$ and showcasing an out-of-plane spin polarization that reverses sign with reversal of the sample magnetization at 30 K (M^+ and M^- , right).

Supplement: Figure 9) to tune the electron wave number perpendicular to the surface, k_z , once through the whole bulk Brillouin zone (Supplement: Table II), reveals no dispersion evidencing the 2D character of the Dirac cone. This is contrary to the lower-lying 3D bulk bands that strongly disperse with photon energy (Figure 2f, arrows). Spin-resolved ARPES of the 2D Dirac cone showcases a helical in-plane spin texture when probed away from the $\bar{\Gamma}$ zone center, i.e., it exhibits the characteristic reversal of spin orientation with the sign of \mathbf{k}_{\parallel} (Figure 2g,i, Supplement: Figure 8). This spin chirality is a key signature of a topological surface state. In addition, a pronounced out-of-plane spin polarization (about 25 %) occurs at the $\bar{\Gamma}$ zone center in the vicinity of E_F in the remanently magnetized sample and reverses sign when the sample is remanently magnetized in the opposite direction (Figure 2j). Such out-of-plane spin texture at $\bar{\Gamma}$ is evidence for a magnetic gap opening at the Dirac point [63]. Combined, the ARPES results demonstrate that MnSb_2Te_4 is a ferromagnetic topological insulator with clear fingerprints of a magnetic gap at $\bar{\Gamma}$. Favorably, the Dirac point of the topological surface state is rather close to E_F . Extrapolation of the observed linear bands, deduced by Lorentzian peak fitting (Figure 2d,h) yields a position of the Dirac point E_D of only 20 ± 7 meV above E_F at 300 K (Supplementary Section VIII).

Since a Dirac point above E_F is not accessible for ARPES, STS is employed to directly assess the ferromagnetic gap formed at $T < T_C$. Figure 3a shows a topography image (height signal in STM) of the MnSb_2Te_4 epilayer together with six STS spectra recorded at 4.3 K at different locations of the surface. All spectra consistently reveal a gap at E_F varying, however, significantly in size. Attributing the energy region of $dI/dV \approx 0$ as gap (Supplementary Section IX), a detailed map of the gap size Δ results that covers a larger surface region (Figure 3b) [64, 65]. The corresponding gap histogram is displayed as inset. The gap size varies in the range 0–40 meV with mean 17 meV exhibiting a spatial correlation length of 2 nm as observed consistently in three distinct areas (Supplement:Figure 11). A corresponding set of dI/dV curves recorded along the dashed line in Figure 3b is depicted in Figure 3c and showcases the small-scale band gap fluctuations. Likely, the spatial variation of Δ is caused by the spatially varying subsurface defect configuration, i.e., by the Mn atoms at Sb lattice sites. Indeed, the gap fluctuations appear on the same length scale as the topographic features in Figure 1b. The average gap center position is only 0.6 meV above E_F (Supplement: Figure 11) with small discrepancy to $E_D - E_F = 20$ meV as determined by ARPES, which might be caused by slightly different growth conditions of the samples,

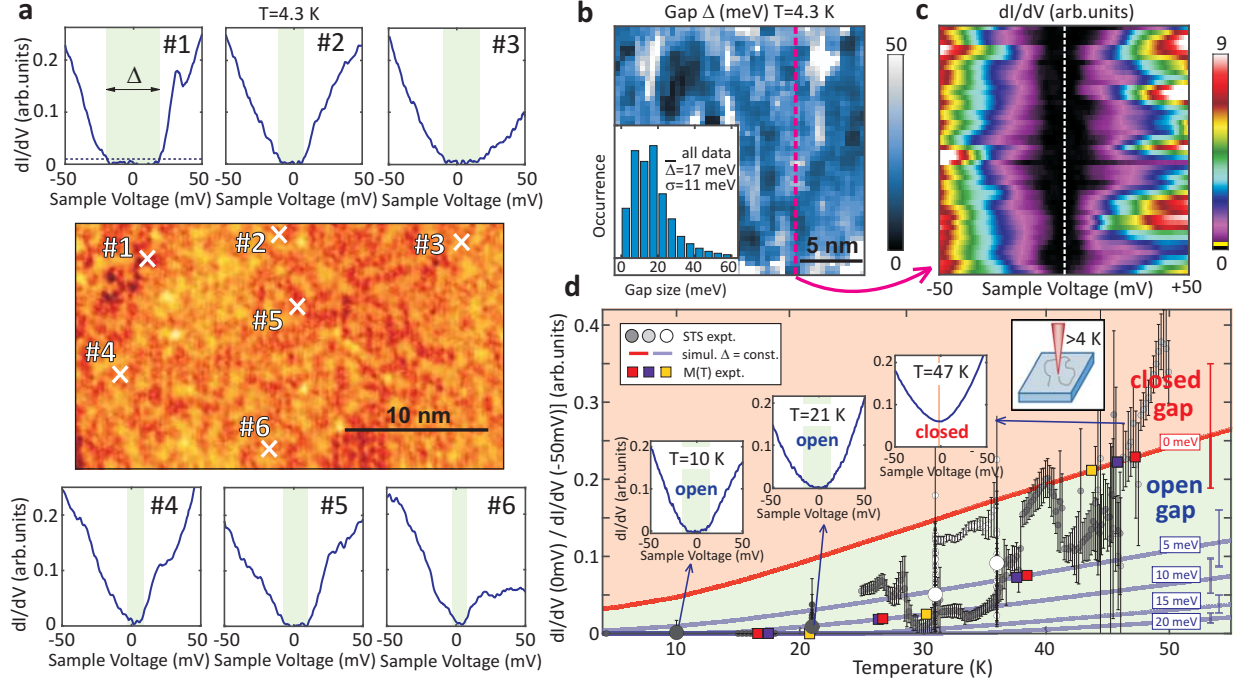


FIG. 3: **Spatial variation of the magnetic energy gap and closing at T_C .** (a) Center: STM image of MnSb_2Te_4 after UHV transfer from the MBE, $V = 0.5$ V, $I = 0.2$ nA, $T = 4.3$ K. Surrounding: dI/dV spectra recorded at the labelled crosses. Dashed line in the upper left spectrum: noise threshold used for determination of gap size Δ (Supplementary Section IX). (b) Spatial map of gap size Δ . Inset: histogram of Δ resulting from three distinct areas, average gap size $\bar{\Delta}$ and standard deviation σ are marked. (c) dI/dV spectra (color code) along the magenta dashed line in (b). Yellow line at the bottom of the color code bar: threshold for gap determination in (a,b). (d) Small dots: Ratio $R = [dI/dV(V=0 \text{ mV})] / [dI/dV(V=-50 \text{ mV})]$ deduced from $dI/dV(V)$ curves at different T . Different grey shades: different cooling cycles. Each point belongs to a single position on the sample surface within 1 nm. Error bars: standard deviation resulting from multiple curves measured at the same position. Large grey dots: average values at the corresponding T representing spatially averaged gap sizes $\bar{\Delta}(21 \text{ K}) = 11 \pm 5$ meV, $\bar{\Delta}(31 \text{ K}) = 6 \pm 1$ meV, and $\bar{\Delta}(36 \text{ K}) = 4 \pm 1$ meV (Supplementary Section IX). Grey lines: T -dependence of the ratio R for the marked gap sizes $\bar{\Delta}$, deduced by convolving the measured $dI/dV(V)$ at 4.3 K with the Fermi distribution (Supplement: Fig. 13b). The area above $\Delta = 0$ meV exhibits such a large R that the existence of a gap is excluded. Error bars on the right mark a standard deviation due to variation of the dI/dV curves at 4.3 K (Supplement: Fig. 13b). Colored squares: gap values deduced from XMCD (yellow, Fig. 1f) and SQUID (red, violet, Supplement: Fig. 7) using $\bar{\Delta}(T) \propto M(T)$ [70]. Insets: selected dI/dV curves for the points with blue arrows. Additional curves: Supplement: Fig. 12

by different temperatures of the two measurements (4.3 K versus 300 K) or by larger-scale potential fluctuations [66, 67].

To prove that the energy gap is of magnetic origin [24], the temperature dependence $\Delta(T)$ is probed by STS. This has not been accomplished yet for any magnetic topological insulator because at higher temperatures $k_B T \geq \Delta/5$ the STS gap Δ is increasingly smeared by the Fermi-Dirac distribution. This leads to a small, i.e., non-zero tunneling current at voltages within the band gap [68]. A direct deconvolution of the local density of states (LDOS) and the Fermi distribution function would require an assumption on the shape of the LDOS as function of energy. Such an assumption is not justified because a significant spatial variation of the dI/dV curves is observed at 4.3 K (Figure 3a–c), as found consistently in other magnetic topological insulators [64, 69]. Therefore, a new method to derive Δ at elevated T is established. For this purpose, the ratio between dI/dV at $V=0$ mV and dI/dV at larger V , outside the region of the band gaps observed at 4.3 K, is employed (Supplementary Section IX D). Figure 3d displays the ratio $R = [dI/dV(0 \text{ mV})]/[dI/dV(-50 \text{ mV})]$ for a large number of dI/dV spectra recorded at temperatures varying from 4.3 K to 50 K (small dots). Selected dI/dV spectra at 10, 21 and 47 K are shown as insets (more dI/dV data in Supplement: Figure 12). One can see that up to 20 K, the STS ratio R is zero and thus $dI/dV = 0$ nS at zero bias, directly evidencing the persistence of the gap. At higher temperatures the R values gradually increase due to the temperature broadening effect along with a decreasing magnetic gap size as the temperature approaches T_C . To separate these two effects, the temperature dependence of the STS ratio for fixed gap sizes $\Delta(4.3 \text{ K}) = 0, 5, 10, 15$ and 20 meV is modelled by convolving the dI/dV curves recorded at 4.3 K (Figure 3a–c) with the Fermi distribution, while capturing their gap sizes Δ (Supplement: Figure 13). The corresponding model results are represented by solid grey lines in Figure 3d, where the red line marked with 0 meV indicates how the STS ratio R evolves with temperature when the gap is zero. Clearly, up to $T = 47$ K, the experimental STS ratios R stay below this line. This evidences that the gap remains open up to T_C whereas above the red line the gap is closed. It directly demonstrates the magnetic origin of the gap [24] due to the ferromagnetism of MnSb_2Te_4 .

Comparing experimental data points with the calculated lines reveals that the gap size continuously decreases as the temperature approaches T_C and closes rather precisely at $T_C = 45\text{--}50$ K in line with the T_C deduced from XMCD and SQUID. As described above, the

gap size varies spatially across the surface (Figure 3a–c) due to local disorder. Accordingly, at higher temperatures the STS ratios also exhibit a considerable variation depending on where the STS spectra were recorded. For this reason, larger ensembles of data points have been recorded at four selected temperatures $T = 10, 21, 31$ and 36 K within an area of 400 nm^2 . From these, the average gap sizes are deduced to $\overline{\Delta}(21 \text{ K}) = 11 \pm 5 \text{ meV}$, $\overline{\Delta}(31 \text{ K}) = 6 \pm 1 \text{ meV}$, and $\overline{\Delta}(36 \text{ K}) = 4 \pm 1 \text{ meV}$, as represented by the large grey and white dots in Figure 3d. Thus, the gap indeed gradually shrinks as the temperature approaches T_C and closes above fulfilling the expectations for a ferromagnetic topological insulator [24]. Note that the different grey shades of the small data points mark different cooling runs starting from an initial elevated temperature. Hence, the tip slowly drifts during cooling across the sample surface while measuring at varying temperature and, thus, explores variations of Δ by T and by spatial position simultaneously. Accordingly, the visible trend of $\Delta(T)$ relies on the sufficient statistics of probed locations that is particularly adequate for the spatially averaged $\overline{\Delta}$ (large dots).

The conclusion that the gap closes at T_C is corroborated by comparing the experimental gap evolution with the measured magnetization $M(T)$ (Figure 1d,f, Supplement: Figure 7) using the relation $\overline{\Delta}(T) \propto M(T)$, as found in previous experiments [24] and theory [70]. Using $M(T)$ from SQUID and XMCD magnetization data (Figure 1d,f, Supplement: Figure 7) and the low temperature gap $\overline{\Delta}(4.3 \text{ K}) = 17 \text{ meV}$ (Figure 3b), one obtains $\overline{\Delta}(T) = \overline{\Delta}(4.3 \text{ K}) \cdot M(T)/M_0$ and, thus, straightforwardly $\overline{R}(T)$ for the magnetization data. The results are presented as yellow, blue and red dots in Figure 3d demonstrating nice agreement to the STS data. This further corroborates the magnetic origin of the gap. Since the center energy of the gap (Supplement: Figure 11f) is close to the estimated Dirac point position in ARPES (Figure 2e,h), the gap is attributed to the topological surface state, consistent with the out-of-plane spin polarization near the Dirac point observed by spin-resolved ARPES (Figure 2j). Such a magnetic gap of a topological surface state close to E_F is highly favorable for probing the resulting topological conductivity and its expected quantization.

To clarify the origin of the discovered ferromagnetic topological insulator, the electronic band structure of MnSb_2Te_4 has been calculated by various DFT methods, considering different magnetic configurations including chemical and magnetic disorder (Supplementary Section XI). As a general result, the topological insulator is reproduced by introducing magnetic disorder. Calculating the bulk band structure, the perfect ferromagnetic system

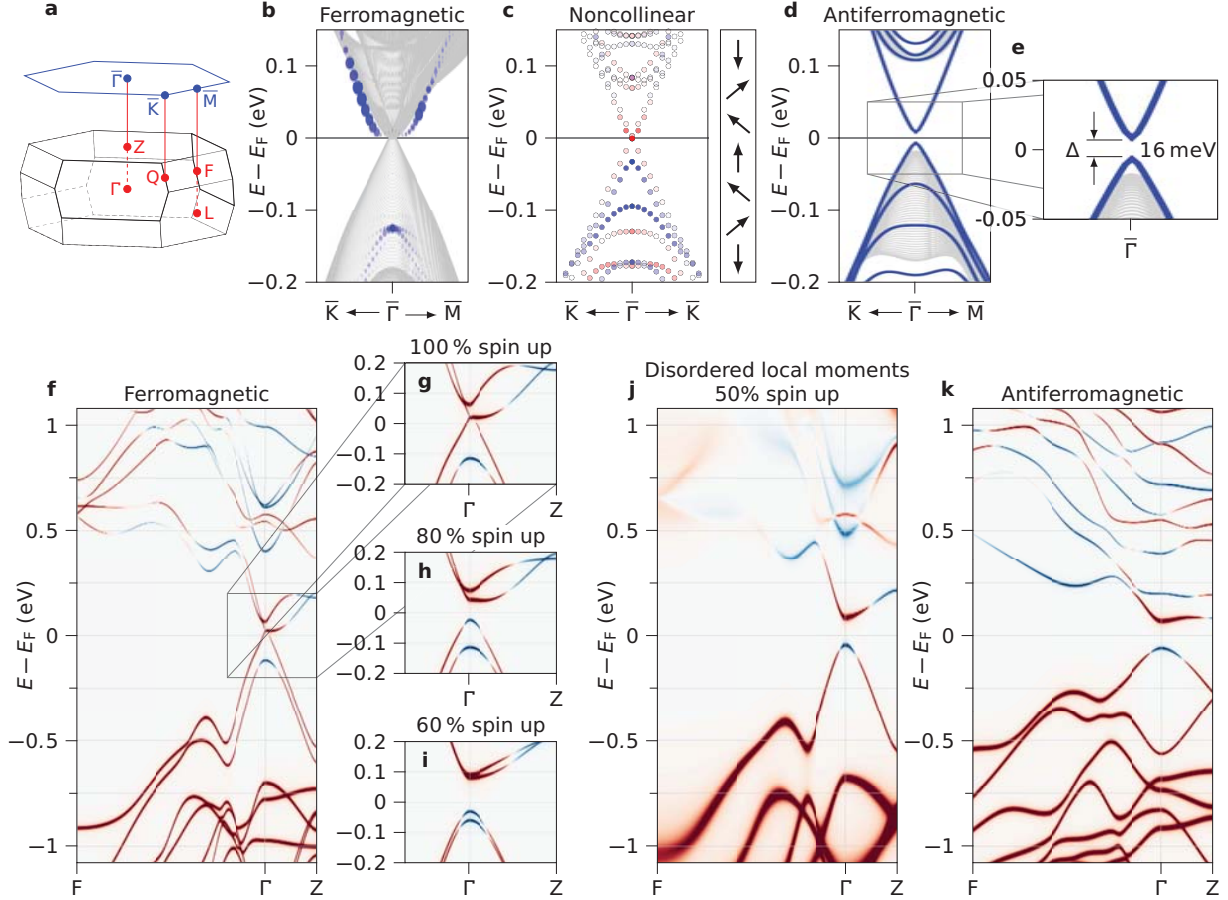


FIG. 4: Theoretical predictions for MnSb_2Te_4 . (a) Brillouin zone of bulk (bottom) and surface (top) of MnSb_2Te_4 with marked high symmetry points. (b–e) Band structures from DFT calculations of slab geometries for various magnetic configurations (marked on top). (b) Ferromagnetic interlayer coupling for a thick slab. Blue dots: surface states identified via their strength in the top septuple layer. (c) Non-collinear interlayer coupling (sketched on the right) for a thin slab. Color code: out-of-plane spin polarization of the gapped Dirac cone. Uncolored circles: bulk states. (d) Antiferromagnetic interlayer coupling for a slab (blue lines) on top of the projected bulk band structure (grey lines) with a gapped Dirac cone at $\bar{\Gamma}$. (e) Zoom into (d) with marked magnetic gap size of the topological surface state. (f–k) Band structures from DFT calculation for a bulk geometry with magnetic configurations as marked on top. Red (blue): dominating anion (cation) character as spectral function difference between anion and cation sites for each state (Supplementary Section XI). (f) Ferromagnetic interlayer coupling with a topologically protected Weyl cone around Γ . (g) Zoom into (f). (h,i) same as (g) but with magnetic disorder modelled via overlap of collinear spin up and spin down states at each Mn site (Supplementary Section XI). (j) Same as (f), but with full magnetic disorder. (k) Antiferromagnetic interlayer coupling. An inverted band gap appears for (h–k) at Γ around E_F visible by the exchanged colors of the two bands, i.e., these structures are topological insulators.

without disorder appears as a topological Weyl semimetal with a zero bulk band gap and a Weyl crossing point located along ΓZ about 5% of the Brillouin zone away from Γ (Figure 4f,g, Supplement: Figures 14e, 15a). This is in agreement with recent calculations [47, 53], but obviously disagrees with the STS and ARPES results. On the other hand, the defect-free *antiferromagnetic* system is found to be a topological insulator with a bulk band gap of 120 meV, Figure 4k. This is evidenced by the band inversion at Γ , indicated by the color code of the spectral function difference between cationic and anionic sites [red (blue): dominating anion (cation) character, Supplementary Section XI]. This color code is also used in Figure 4f–j. Slab calculations of the band structure (Figure 4d) indeed reveal the topological surface state with gap at the Dirac point due to time reversal symmetry breaking. Discrepancies to earlier calculations [51, 52] are discussed in Supplementary Section XIC order, we additionally study deviations from defect-free, pure ferromagnetic or antiferromagnetic order. For more realistic modelling, more complex magnetic orders are taken into account deviating from perfect ferromagnetic or antiferromagnetic order as implied by the magnetometry results (Figure 1e, Supplement: Figure 7). The extreme case of completely disordered local magnetic moments, without net magnetization, showcases a bulk band gap of 135 meV with nontrivial topology as seen from the band inversion around the gap close to Γ (Figure 4j). Varying the degrees of magnetic disorder shows

that already 20% of magnetic disorder breaks up the Weyl point of the ferromagnetic MnSb_2Te_4 and opens an inverted band gap (Figure 4g–i, Supplement: Figure 15). This nontrivial topology induced by magnetic disorder is robust against chemical disorder as Mn-Sb site exchange that proved to be essential for inducing the ferromagnetic order in the system (Supplement: Table III). Indeed, a Mn-Sb site exchange by 5% does not affect the band topology (Supplement: Figure 14). This implies that, contrary to recent conclusions [54], defect engineering accomplishes simultaneously a nontrivial topology and very high Curie temperature for the MnSb_2Te_4 system.

To further assess the robustness of the magnetic gap, slab calculations are employed with various magnetic disorder configurations. The simplest case of a purely ferromagnetic slab does not lead to a Dirac cone, since the bulk band gap vanishes (Figure 4b). The pure antiferromagnetic order, on the other hand, creates a pronounced Dirac cone with magnetic gap of 16 meV, Figure 4d,e, nicely matching the average gap size found by STS (Figure 3b). The magnetic gap size turns out to be a rather local property caused by the exchange

interaction in near-surface MnSb_2Te_4 septuple layers. Naturally, the gapped Dirac cone forms also when the surface of an antiferromagnet is terminated by a few ferromagnetic layers (Supplement: Figure 16d). A relatively strong out-of-plane spin polarization at the gap edges ($\sim 60\%$) is found in that case nicely matching the results of the spin-resolved ARPES data measured at 30 K ($\sim 25\%$), if one takes into account the temperature dependence of the magnetization (Figure 1d,f). Moreover, for more random combinations of antiferromagnetic and ferromagnetic layers, the Dirac cone with magnetic gap persists, albeit the bulk band gap vanishes due to the more extended ferromagnetic portions in that structure (Supplement: Figure 16a). Finally, for a system where the magnetic moments of adjacent septuple layers are continuously tilted with respect to each other, a gapped Dirac cone was also observed, Figure 4c. Likewise, alternate rotations of adjacent collinearly coupled Mn layers by relative angles $\geq 40^\circ$ open a gap in the Weyl cone (Supplement: Figure 15c-f). Hence, magnetic disorder turns out to be a rather universal tool to accomplish topological insulator properties for MnSb_2Te_4 .

Last but not least, it is noted that the slope of the temperature dependent $M(T)$ shows a remarkable linear behavior towards T_C , described by an effective critical exponent $\beta = 0.7-1.2$. This large β apparently persists for about half of the range between $T = 0$ K and T_C (Figure 1d,f). Such large β values do not exist in any classical model ranging from $\beta \simeq 0.125$ for the 2D Ising model to the mean-field value of 0.5. The behavior at the classical critical point may, however, strongly change due to quantum fluctuations, which can lead to $\beta = 1$ in the presence of disorder [71] as experimentally observed [72, 73]. Note that such disorder is witnessed in our samples by the spatial gap size fluctuations (Figure 3). Moreover, the magnetic phases of MnSb_2Te_4 are indeed energetically very close to each other according to DFT [27] as also indicated by the kink in the $M(T)$ curve (Supplement: Figure 7, top).

In summary, high quality epitaxial MnSb_2Te_4 films with regularly stacked Te-Sb-Te-Mn-Te-Sb-Te septuple layers and a small Mn excess located in the Sb layers feature a robust nontrivial band topology at record high Curie temperatures. DFT based band structure calculations, ARPES and STS experiments showcase a 2D Dirac cone as nontrivial topological surface state with a magnetic gap of ~ 17 meV located very close to E_F . The gap disappears at T_C and above, signifying its magnetic origin as corroborated by an out-of-plane spin polarization at the Dirac point found by ARPES. by out-of-plane spin polarization at the Dirac point found by ARPES. We thus conclude that the smaller spin-orbit interaction in

MnSb₂Te₄ as compared to MnBi₂Te₄ is still sufficient to maintain both, the band inversion and the perpendicular magnetic anisotropy, provided that some Mn resides in the Sb layers. The discovered properties are highly favorable for the quantum anomalous Hall effect and other topology-based device applications as the critical temperature is twice as large as for MnBi₂Te₄ and the Dirac point is close to E_F with small spatial variation.

Hence, the smaller spin-orbit interaction in MnSb₂Te₄ as compared to MnBi₂Te₄ is still sufficient to maintain both the band inversion and the perpendicular magnetic anisotropy in the case of a slight Mn excess. Ferromagnetism is triggered by a new balance of exchange interactions induced by a few percent of Mn-Sb site exchange in the Sb layers in combination with a slight in-plane contraction as deduced by combining DFT, RBS, STM and XRD results. The DFT calculations indicate that magnetic disorder is essential for the magnetic topological insulator phase. Indeed, the magnetization features an exotic critical exponent $\beta \approx 1$ which indicates the influence of a quantum critical point, likely merging ferromagnetic and antiferromagnetic order.

Acknowledgements

We are indebted to Ondrej Man for help with lamella preparation for TEM. Financial support from the Austrian Science Funds (Projects No. P30960-N27 and I3938-N27), the Impuls-und Vernetzungsfonds der Helmholtz-Gemeinschaft under grant No. HRSF-0067 (Helmholtz-Russia Joint Research Group), the CzechNanoLab project LM2018110 funded by MEYS CR, the CEITEC Nano Research Infrastructure, the Swedish Research Council (Project No. 821-2012-5144), the Swedish Foundation for Strategic Research (Project No. RIF14-0053), the Spanish Ministerio de Ciencia e Innovación (Project No. PID2019-103910GB-I00), Tomsk State University (Project No. 8.1.01.2018), and Saint Petersburg State University (Project No. 51126254) are gratefully acknowledged. The work was also funded by the Deutsche Forschungsgemeinschaft within SPP1666 Topological Insulators and Germany's Excellence Strategy — Cluster of Excellence Matter and Light for Quantum Computing (ML4Q) EXC 2004/1 — 390534769, and the project Mo 858/13-2 as well as by the Graphene Flagship Core 3.

Supplementary Sections

The following sections describe the experimental and theoretical methods as well as additional data supporting the conclusions from the main text.

I. SAMPLE GROWTH

MnSb₂Te₄ films were grown by molecular beam epitaxy (MBE) on BaF₂(111) substrates using a Varian GEN II system. Compound Sb₂Te₃ and elemental Mn and Te sources were employed for control of stoichiometry and composition. Typical sample thicknesses were 200 nm. Deposition was carried out at a sample temperature of 290°C at which perfect 2D growth is sustained independently of the Mn concentration, as verified by *in situ* reflection high energy electron diffraction and atomic force microscopy. The flux rates were calibrated by quartz microbalance measurements. For angle-resolved photoelectron spectroscopy (ARPES) performed at BESSY II and for scanning tunneling microscopy (STM) performed at RWTH Aachen University, samples were transferred from the MBE system by an ultrahigh vacuum (UHV) suitcase that allowed transportation without breaking UHV conditions. Samples used for magnetometry and x-ray magnetic circular dichroism (XMCD) were capped *in situ* after growth with amorphous Se and Te capping layers to protect the surface against oxidation.

II. ELECTRON MICROSCOPY

High-resolution scanning transmission electron microscopy (TEM) was performed with a FEI Titan 60-300 Themis instrument equipped with a Cs image corrector. The TEM data were recorded with a high-angle annular dark field (HAADF) detector and the images processed using a fast Fourier transform and Fourier mask filtering technique for noise minimization. Thin cross-sectional lamellae from MnSb₂Te₄ films were prepared by focused ion beam milling (FEI Helios NanoLab 660).

III. RUTHERFORD BACKSCATTERING

The chemical composition of the samples was determined by Rutherford backscattering spectrometry (RBS) employing a primary beam of 2 MeV ⁴He⁺ ions provided by the 5 MV 15SDH-2 Pelletron accelerator at Uppsala University. A solid-state detector was placed in backscattering geometry under an angle of 170° with respect to the primary beam. The beam incidence angle was randomized in a 3° angular interval around an equilibrium angle of 18° with respect to the surface normal to counteract potential channeling effects. The

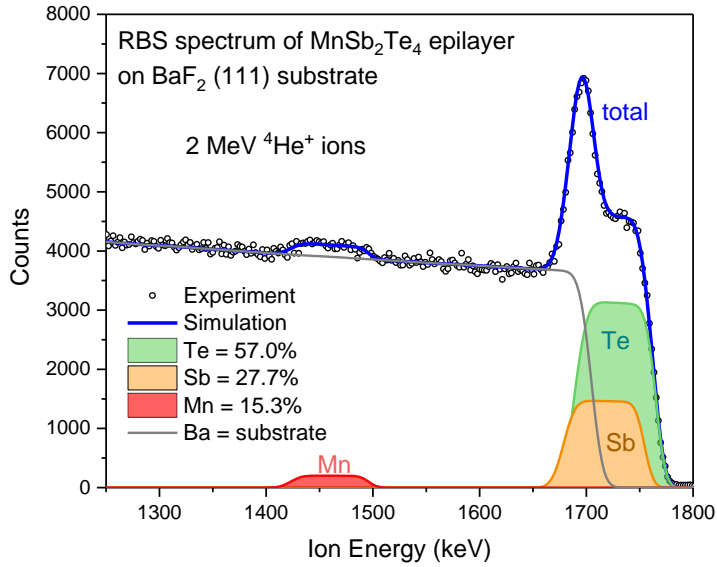


FIG. 5: **Chemical composition and depth profile.** Rutherford backscattering spectrum (open circles) measured in random geometry. The simulation of the total backscattering signal using SIMNRA (blue line) is in excellent agreement with the experimental data. The corresponding contributions of the film constituents (Te, Sb and Mn) are marked and indicated by the green, orange and red lines surrounding correspondingly shaded areas. The data reveal a slight Mn excess of $\sim 7\%$ and an Sb deficiency of $\sim 3\%$ with respect to the ideal MnSb_2Te_4 stoichiometry suggesting a partial Mn replacement of Sb atoms in the Sb layer.

resulting spectra (Fig. 5) were fitted by the SIMNRA software package [74] to obtain the film composition and confirm its uniformity over the film cross section. Analysis of the RBS data as shown in Fig. 5 yields an excellent fit (blue line in Fig. 5) for atom concentrations of 57.0% Te, 27.7% Sb and 15.3% Mn with a high uniformity throughout the film cross section. The composition is close to the nominal MnSb_2Te_4 stoichiometry, but features a slight Mn excess of $\sim 7\%$ and a slight Sb deficiency of $\sim 3\%$ indicating the substitution of Sb atoms in the Sb layers by additional Mn atoms as corroborated by the x-ray diffraction data shown in section IV.

IV. X-RAY DIFFRACTION

The crystalline structure was determined by x-ray diffraction (XRD) scans and reciprocal space maps recorded in the vicinity of the $(10\bar{1}.20)$ reciprocal lattice point. The measure-

ments were performed using a Rigaku SmartLab diffractometer with Cu x-ray tube and channel-cut Ge(220) monochromator. The results are shown as red lines in Fig. 6. The symmetric scans along the $[000.1]$ reciprocal space direction (c -axis) were fitted with a modified one dimensional paracrystal model [24, 75] (black lines in Fig. 6). We have fitted the data of two samples and obtained consistent results of $a = 4.23 \text{ \AA}$ and $c = 40.98 \text{ \AA}$.

We modelled the Mn-Sb site exchange by different Mn occupancies C_1 and C_2 within the central cation lattice planes, usually assumed to be occupied by Mn only, and within the outer cation lattice planes, usually assumed to be occupied by Sb only, respectively. For that purpose, the structure factor of MnSb_2Te_4 reads

$$F(Q_z) = \sum_n C_n f_n(Q_z) \exp(-iQ_z z_n), \quad (1)$$

where $f_n(Q_z)$ is the atomic form factor of the n -th atom in the unit cell, z_n its coordinate, C_n its occupancy, Q_z its position in reciprocal space and the summation runs over all atoms in the septuple layer. For Sb, Te, and Mn the atomic form factors at $Q_z = 0.9 \text{ \AA}^{-1}$ are 48.9, 49.9 and 23.6, respectively.

The fit result that assumes the ideal septuple layer structure with regular layer sequence Te-Sb-Te-Mn-Te-Sb-Te ($C_1 = 1$, $C_2 = 0$) is shown on the bottom of Fig. 6a, while $C_1 = 0.6$ and $C_2 = 0.4$, corresponding to 60% of the Mn atoms in the central septuple layer and 40% in the outer two cation layers, is shown on top. Figure 6b highlights the low Q_z region featuring the strong sensitivity of the peak at $Q_z = 0.9 \text{ \AA}^{-1}$ to the exchange of Mn and Sb. For this peak, the two different cation layers contribute to the structure factor with almost exactly opposite phase, while the contribution of the Te layers almost cancels. Because of the different Mn and Sb atomic form factors, the intensity of this peak rapidly diminishes with increasing Mn-Sb exchange and completely vanishes for $C_1 = C_2 = 0.5$. The best fit to the experiment is found for $C_1 = 0.9 \pm 0.1$ and $C_2 = 0.1 \pm 0.1$ evidencing a non-ideal distribution of Mn and Sb in the respective layers.

V. MAGNETOMETRY BY SQUID

The magnetic properties were determined by a superconducting quantum interference device (SQUID) magnetometer (Quantum Design MPMS-XL) as a function of temperature from 2 K to 300 K. The external field \mathbf{H} was applied either parallel (in plane) or perpen-

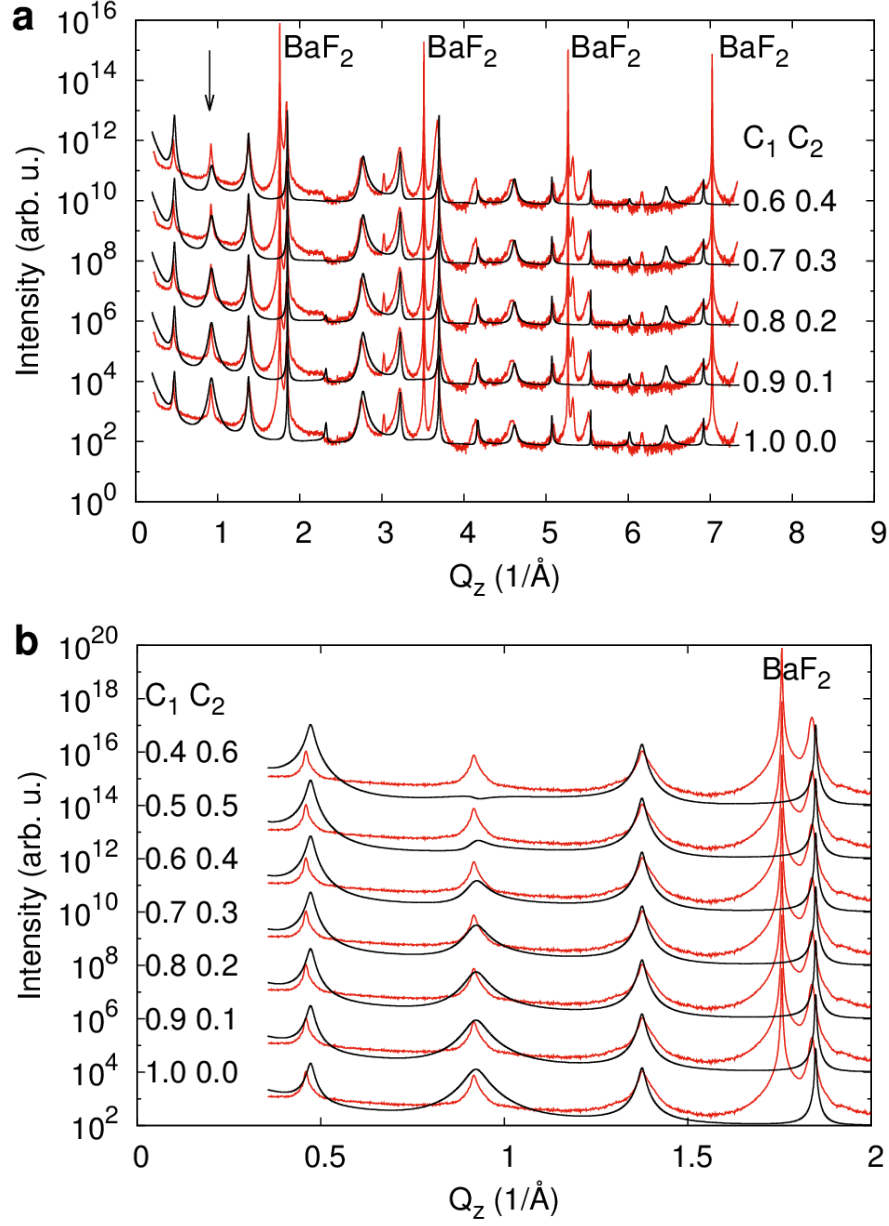


FIG. 6: **X-ray diffraction spectra with fits.** (a) Experimental x-ray diffraction spectrum of the MnSb_2Te_4 epilayer (red lines) compared with simulations (black lines) using a one-dimensional paracrystal model [24, 75] while assuming different Mn occupation in the central layer (C_1) and in the adjacent cation layers (C_2) of the septuple layer. (b) Zoom into (a) showcasing the strong sensitivity of the peak at $Q_z \approx 0.9 \text{ \AA}^{-1}$ (black arrow in (a)) to the Mn-Sb site exchange. Peaks of the BaF_2 substrate are marked.

dicular (out of plane) to the epilayer surface, that itself is oriented perpendicular to the crystallographic c axis. The diamagnetic contribution of the substrate was determined from the slope of the magnetization $M(H)$ recorded at high magnetic fields and 300 K well above the Curie temperature T_C of MnSb_2Te_4 , where the magnetic contribution of the thin film is completely superseded by that of the thousand times thicker substrate. The derived substrate contribution was then subtracted from the raw data recorded at lower T . Identical sample pieces were used for in-plane and out-of-plane measurements.

Figure 7 shows out-of-plane $M(T)$ data while field cooling at 10 mT for three different samples. They reveal a quite similar T_C and consistently display a ferromagnetic behavior via its remanence. Data for sample 1 are also shown in Fig. 1 (main text) where they give a slightly smaller T_C within the error bars.

Figure 7 (top) features a small kink at 20–25 K that indicates deviations from pure ferromagnetic order possibly indicating a second phase transition that might contribute to the large critical exponent $\beta \simeq 1$ as discussed in the main text and attributed there to the vicinity to a quantum critical point.

VI. COMPARISON WITH MAGNETIC PROPERTIES OF OTHER MNSB_2TE_4 SAMPLES

Table I compares the results of our three MnSb_2Te_4 samples with data from the literature. The comparison highlights the exceptionally large Curie temperature of the Mn-rich epitaxial films.

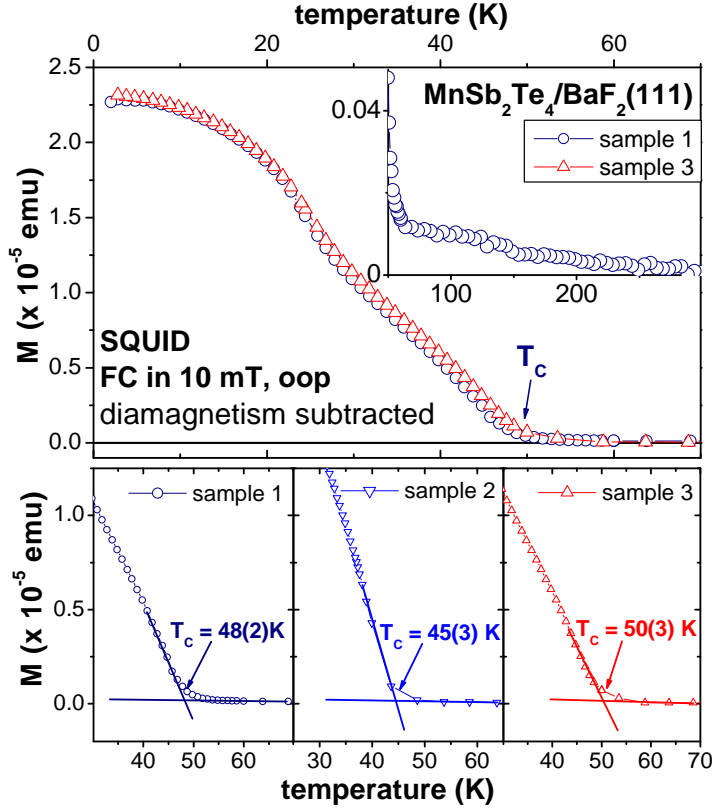


FIG. 7: **Magnetometry by SQUID.** Magnetization $M(T)$ of three individual MnSb_2Te_4 epilayers measured by SQUID. $M(T)$ was measured in out-of-plane (oop) direction while field cooling (FC) in a field of 10 mT. Linear extrapolation to $M = 0$ emu was used to estimate T_C as marked. Notice the small kink in $M(T)$ around 20 K in the top panel which indicates deviations from pure ferromagnetic order. Inset: Full temperature dependence of the magnetization $M(T)$ up to 300 K on a vertical scale enlarged by a factor of 40. From the SQUID raw data, the diamagnetic contribution from the BaF_2 substrate of $0.0205 \mu\text{emu/Oe}$ was subtracted.

VII. RESONANT SCATTERING AND X-RAY CIRCULAR DICHROISM

Resonant scattering and XMCD were measured at the extreme ultraviolet (XUV) diffractometer of the UE46-PGM1 undulator beam line of BESSY II at Helmholtz-Zentrum Berlin. The XMCD signal was obtained by measuring the difference of the (0001) Bragg peak intensities for incident photons with opposite circular polarization and the photon energy tuned to the $\text{Mn-}L_3$ resonance. In this setup, the sample was field cooled down to 10 K in an external field of about 0.5 T provided by a removable permanent magnet. Subsequent po-

nominal stoichiometry	growth	magnetism	critical temperature	reference
MnSb ₂ Te ₄	epitaxial film	FM	T _C =46-48 K	sample 1, this work
MnSb ₂ Te ₄	epitaxial film	FM	T _C =45 K	sample 2, this work
MnSb ₂ Te ₄	epitaxial film	FM	T _C =50 K	sample 3, this work
MnSb ₂ Te ₄	single crystal	AFM	T _N = 19 K	J.-Q. Yan et al. ^{a)}
MnSb ₂ Te ₄	single crystal	AFM	T _N =19.5 K	Y. Chen et al. ^{b)}
MnSb _{1.8} Bi _{0.2} Te ₄	single crystal	FM	T _C =26 K	Y. Chen et al. ^{b)}
MnSb ₂ Te ₄	polycrystal	FM	T _C =25 K	Murakami et al. ^{c)}

TABLE I: **Magnetic properties of MnSb₂Te₄** for epitaxial films, bulk crystals and polycrystals, comparing the ferromagnetic (FM) Curie temperatures T_C determined in the present work to T_C and antiferromagnetic (AFM) Néel temperatures T_N from the literature. ^{a)} J.-Q. Yan et al., Phys. Rev. B 100, 104409 (2019); ^{b)} Y. Chen et al., Phys. Rev. Mat. 4, 064411 (2020); ^{c)} T. Murakami et al., Phys. Rev. B 100, 195103 (2019).

larization dependent and wave-vector dependent measurements were performed in zero field at various temperatures. The recorded XMCD data are thus a direct measurement of the remanent ferromagnetic polarization of the Mn moments in MnSb₂Te₄.

VIII. ARPES AND SPIN-RESOLVED ARPES

ARPES measurements were performed at 30 K with a Scienta R4000 hemispherical analyzer at the RGBL-2 end station of the U125/2 undulator beamline at BESSY II. Light is incident under an azimuthal angle of 45° and a polar angle of 90° with respect to the sample surface. The light polarization is linear and horizontal. Photon energies between 19 and 70 eV were employed. Spin-resolved ARPES spectra were acquired with a Mott-type spin polarimeter operated at 25 kV, capable of detecting both in-plane and out-of-plane spin components. Samples were transported to the RGBL-2 setup in a UHV suitcase to always maintain pressures below $1 \cdot 10^{-10}$ mbar. Overall resolution of ARPES measurements was 10 meV (energy) and 0.3° (angular). Resolutions for spin-resolved ARPES were 45 meV

(energy) and 0.75° (angular).

For the measurement in Fig. 2j, main text, the sample was magnetized in situ at 30 K by applying a pulsed magnetic field from a removable coil of $\sim \pm 0.5$ T in the direction perpendicular to the surface. As usual, the spin-resolved ARPES experiment is conducted in remanence. The movement between the ARPES chamber and the preparation chamber, where the coil is situated, is a vertical movement of the cryostat so that the sample is always at 30 K.

Figure 8 shows a complete set of spin-polarized ARPES data featuring all three orthogonal spin directions for a finite $k_{\parallel} = \pm 0.15 \text{ \AA}^{-1}$. Only in-plane spin polarization perpendicular to the electron wave vector k_{\parallel} appears and reverses sign with a sign change of k_{\parallel} . This evidences a spin texture that rotates anti-clockwise (right-handed) around the measured Dirac cone (Fig. 2g,i, main text) with the electron spin locked to the electron momentum. Such helical in-plane spin texture is a key signature of the topological character of the Dirac cone. Note that the ferromagnetism of MnSb_2Te_4 exhibits out-of-plane anisotropy such that bulk states cannot have in-plane spin polarization, which fully supports the assignment to the Dirac cone surface state. To deduce the Dirac point energy E_D , the peaks within momentum distribution curves are fitted by two Lorentzians (Fig. 8e) and the energy dependent peak maxima are connected via two fitted lines (Fig. 8d and Fig. 2d,h, main text) that cross at $E_D - E_F = 20 \pm 7 \text{ meV}$. The binding energy range of the fit was determined by the possibility to fit separate Lorentzians, see Fig. 8d,e. Since we do not observe any surface band bending by residual gas adsorption (prominent for the n-doped systems such as Bi_2Se_3 and Bi_2Te_3), the Dirac point can be regarded as a rather good measure of the chemical potential.

Figure 9 shows that the Dirac cone surface state has no dispersion with the wave vector perpendicular to the surface plane, in contrast to the bulk valence band. Figure 9 is the input for Fig. 2b, main text, with linear interpolation between the 9 photon energies. Table II shows the momentum values in kinetic energy.

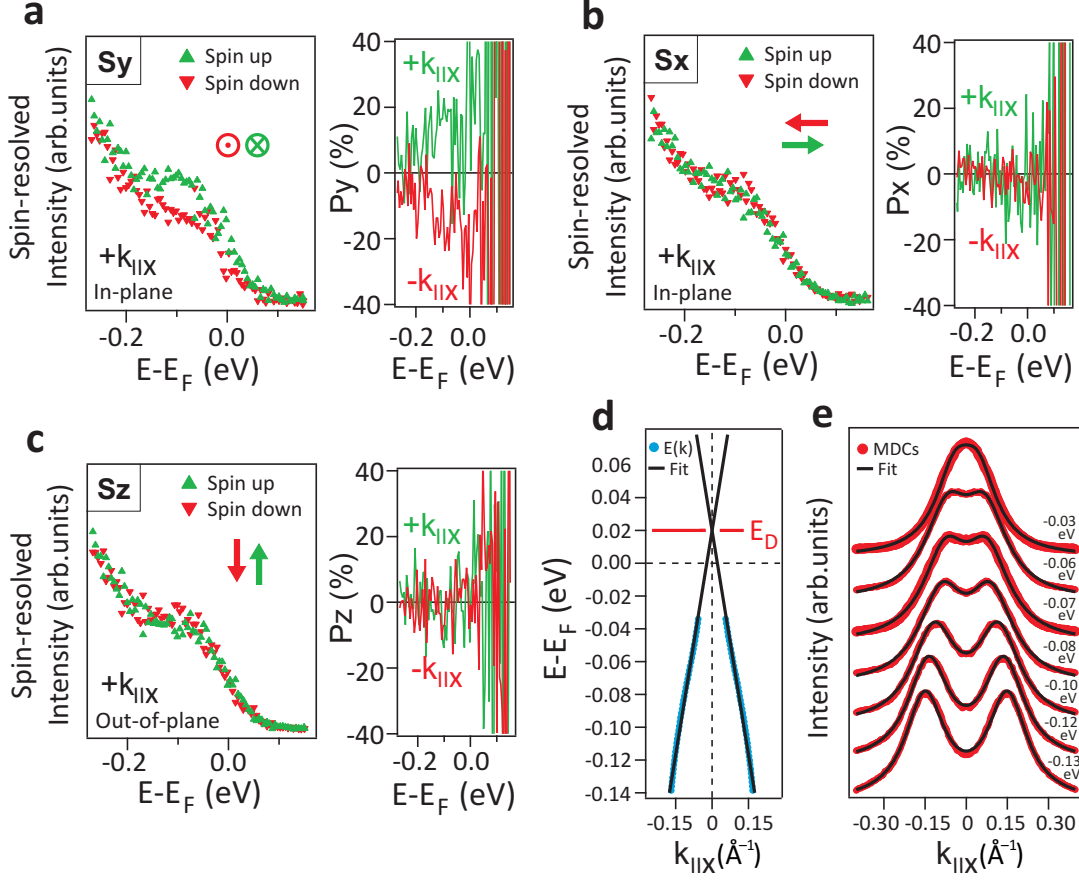


FIG. 8: **Spin-resolved ARPES data and fit of Dirac cone.** All three spin polarization components are shown for $k_{||,x} \simeq \pm 0.15 \text{\AA}^{-1}$ (indicated in Fig. 2h, main text). Left hand side of each subfigure shows the ARPES data for the two opposite spin channels at $k_{||,x} \simeq +0.15 \text{\AA}^{-1}$, while the right hand side shows the resulting spin polarization P_i for both $k_{||,x} \simeq \pm 0.15 \text{\AA}^{-1}$. (a) In-plane spin components perpendicular to $k_{||,x}$ (same as Fig. 2g, main text). (b) In-plane spin components parallel/antiparallel to $k_{||,x}$. (c) Out-of-plane spin components. The symbols for spin direction and orientation are relative to panel (d). (d) The Dirac energy E_D is determined by the crossing of two lines given by fits to experimental data points which, in turn, were determined by Lorentzians fitted to momentum distribution curves (MDC). These fits are shown in panel (e). $h\nu = 25 \text{ eV}$.

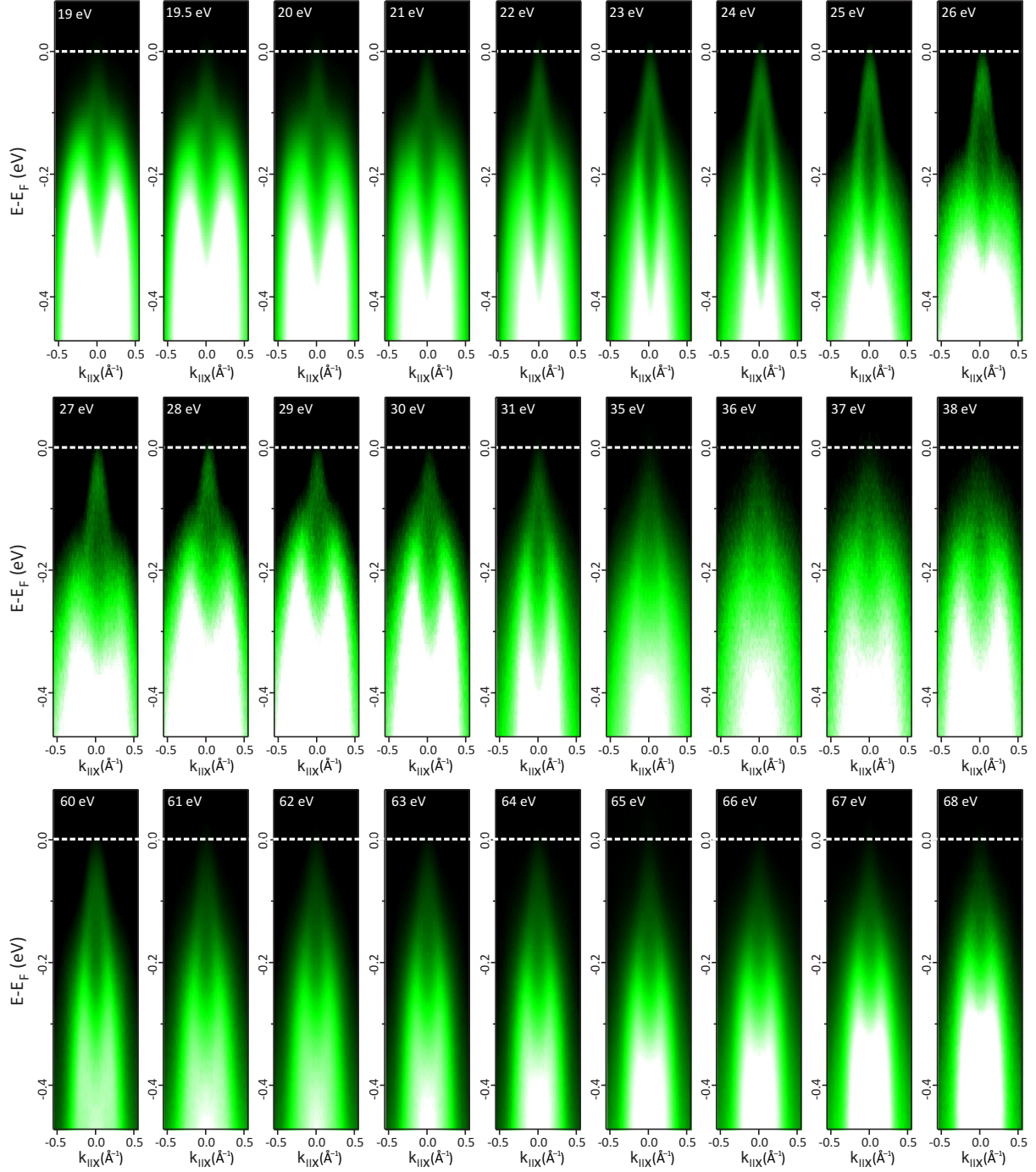


FIG. 9: **Photon-energy-dependent ARPES data.** Energy-momentum dispersions for photon energies from 19 to 68 eV showing a 2D Dirac cone and the dispersion of 3D bulk states with photon energy. The periodicity in the bulk dispersion demonstrates that the bulk Brillouin zone is probed completely.

hv (eV)	$k_z(\text{\AA}^{-1})$
60	4.341
61	4.371
62	4.401
63	4.431
64	4.460
65	4.490
66	4.519
67	4.548
68	4.576

TABLE II: **Perpendicular momentum.** Determination of the perpendicular momentum for the data shown in Fig. 2a,b, main text. Distance from Γ to Z corresponds to 0.1327 \AA^{-1} . An inner potential of 11.8 eV was used.

IX. SCANNING TUNNELING MICROSCOPY AND SPECTROSCOPY

A. Measurement Details

STM measurements were conducted in a home built UHV-STM operating down to $T = 4.3\text{K}$. Cr tips were firstly etched ex-situ and additionally prepared in UHV by field emission on clean W(110). Topography images were recorded in constant-current mode at a tunneling current I and bias voltage V applied to the sample. The $dI/dV(V)$ spectra for scanning tunneling spectroscopy (STS) were recorded after firstly stabilizing the tip-sample distance at voltage $V_{\text{Stab}} = -0.1\text{V}$ and current $I_{\text{Stab}} = 0.1\text{nA}$, if not mentioned differently in the captions. Afterwards, the feedback loop was opened and dI/dV was recorded using standard lock-in technique with modulation frequency $f = 1219\text{Hz}$ and amplitude $V_{\text{mod}} = 1.4\text{mV}$ while ramping V . The spectra were normalized to account for remaining vibrational noise during stabilization by equilibrating the integral between V_{Stab} and $V = 0\text{mV}$. We crosschecked that dI/dV curves barely depend on the chosen I_{stab} and, hence, on the tip-surface distance (Fig. 10).

For measurements above the base temperature of 4.3 K, the STM body was exposed

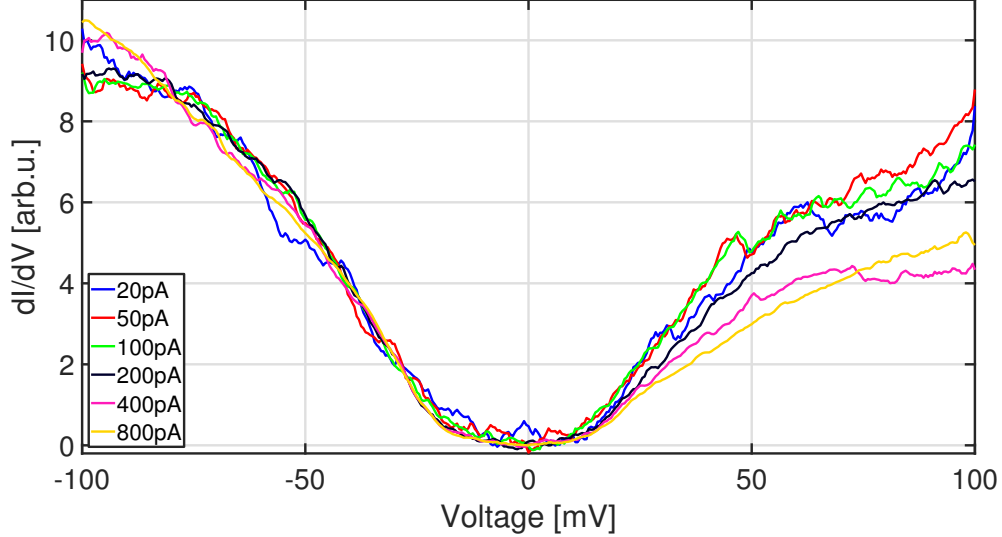


FIG. 10: **STS curves recorded at different set points.** $dI/dV(V)$ curves recorded at the same position after stabilizing the tip at $V_{\text{stab}} = -100$ mV and various I_{stab} as marked, $T = 4.3$ K.

to thermal radiation via opening of a radiation shield until a maximum $T \simeq 60$ K was achieved. Then, the shield was closed, and $dI/dV(V)$ curves were recorded while the sample temperature slowly decreased back to 4.3 K. Measurements at constant $T > 4.3$ K were performed with partly open shield. A more frequent stabilization between subsequent dI/dV curves was necessary due to the remaining thermal drift of the tip-sample distance during the cooling process. This implies shorter recording times that have been compensated by a more intense averaging of subsequently recorded curves.

B. Band Gap Determination at 4.3 K

The band gaps at $T = 4.3$ K were determined as follows. First, the noise level of the dI/dV curves was reduced by averaging 3×3 curves covering an area of $(1.2 \text{ nm})^2$. Subsequently, an averaging of $dI/dV(V)$ across ± 2 mV in bias direction was employed. Then, we estimated the remaining dI/dV noise level as the maximum of $|dI/dV|$ that appears with similar strength positively and negatively. For that purpose, we employed about 50 randomly selected $dI/dV(V)$ curves. Afterwards, the threshold was chosen slightly above the determined noise level. This threshold is marked in Fig. 3a #1 as dashed line and in Fig. 3c as yellow line in the color code bar. The voltage width, where the $dI/dV(V)$ spectra stayed below this threshold, defines the measured gap Δ as used in Fig. 3a–c, main text.

We crosschecked that dI/dV values below the noise level appeared exclusively close to the determined band gap areas. The resulting gap size Δ turned out to barely depend on details of the chosen noise threshold.

Figure 11a and b display two additional $\Delta(x, y)$ maps like the ones in Fig. 3b, main text, but recorded on different areas of the sample surface. They exhibit a similar range of spatial fluctuations of Δ as shown in Fig. 3b, main text. Sometimes, Δ could not be determined from the $dI/dV(V)$ curves as, e.g., in the bright area marked by a black circle in Fig. 11a. There, the spectra stayed below the threshold on the positive $V > 0$ mV side up to 100 mV while a gap edge is observed only on the negative side, for an unknown reason. These spectra ($\sim 5\%$ of all spectra) are discarded from further analysis including the histogram of Fig. 3b, main text. The correlation length ξ of $\Delta(x, y)$ is calculated as FWHM of the correlation function resulting in $\xi \simeq 2$ nm as given in the main text.

The central energy within the gap, E_0 , is deduced as the arithmetic mean of all voltages where the dI/dV signal remains below the threshold. Figure 11c–f displays maps $E_0(x, y)$ for the three studied areas as well as a resulting E_0 histogram. Favorably, the average of E_0 is rather precisely at E_F showing only small spatial fluctuations in the meV range. The small discrepancy of the average $E_0 \simeq E_F$ found by STS to the Dirac point determined by ARPES (20 meV above E_F) might be due to the different recording temperatures (4.3 K vs. 300 K) or to sample to sample variations.

C. $dI/dV(V)$ Curves at Different Temperatures

Figure 12 displays $dI/dV(V)$ spectra recorded at various temperatures as used for the band gap evaluation displayed in Fig. 3d, main text. An obvious band gap with a voltage region of $dI/dV \simeq 0$ nS is only found up to about 30 K. At larger T , the curves partly stay close to $dI/dV = 0$ nS around E_F , but partly strongly deviate from $dI/dV = 0$ nS. This varying behaviour requires a more detailed analysis to determine Δ , since a small deviation from $dI/dV = 0$ nS might also be caused by Fermi level broadening of the tip that probes a local density of states (LDOS) of the sample with a small band gap.

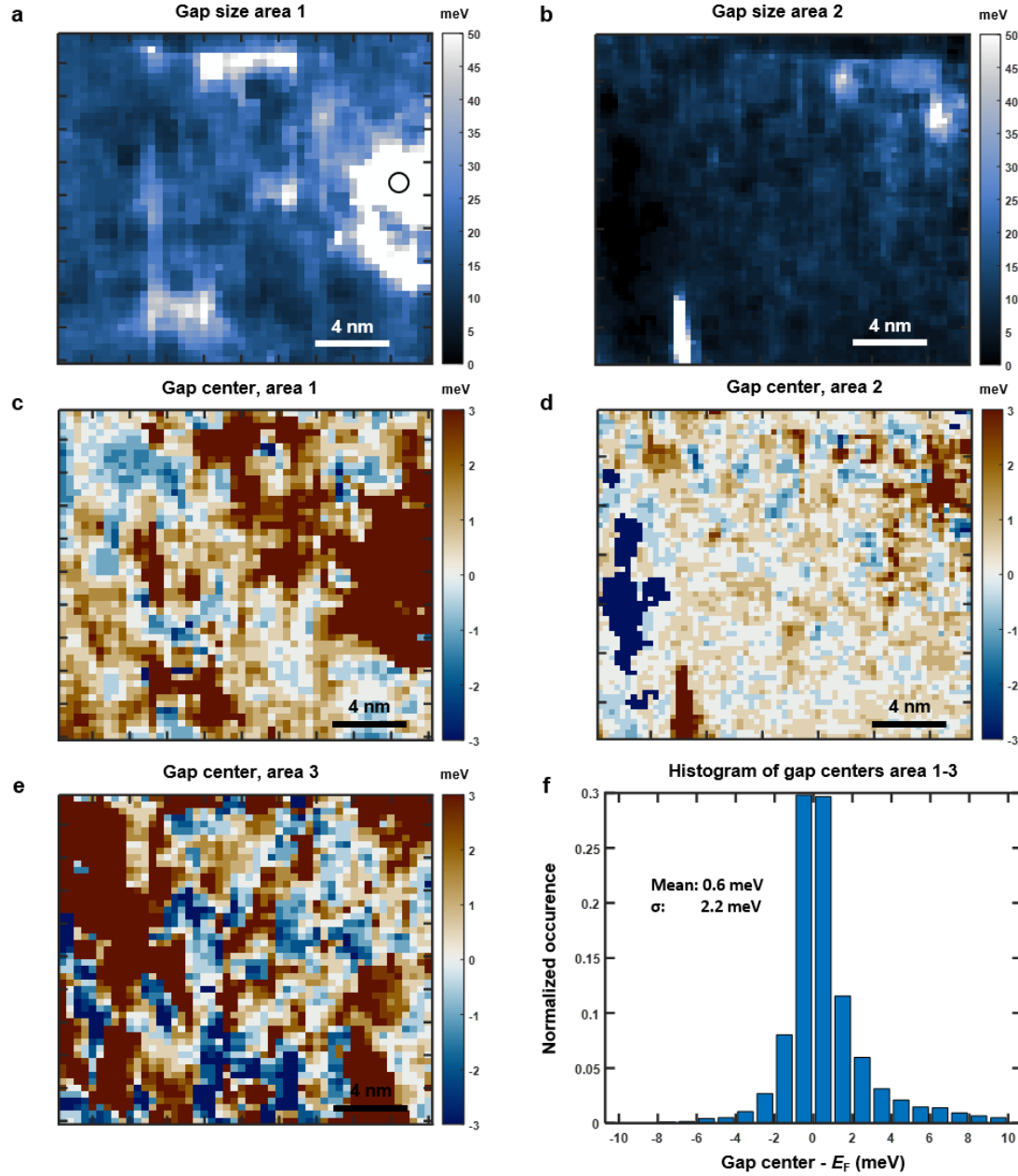


FIG. 11: Maps of gap size Δ and gap center E_0 at 4.3 K. (a,b) Spatial maps of the gap size $\Delta(x, y)$ as obtained from $dI/dV(V)$ curves recorded at $T = 4.3$ K. Two additional surface areas named area 1 and area 2 are shown, while area 3 is displayed in Fig. 3b, main text. The black circle marks a region, where the determination of a band gap was not possible (see text). (c)-(e) Spatial maps of the center of the gap $E_0(x, y)$ with respect to the Fermi level E_F for the 3 different areas. (f) Histogram of E_0 for all three maps with marked mean and standard deviation σ .

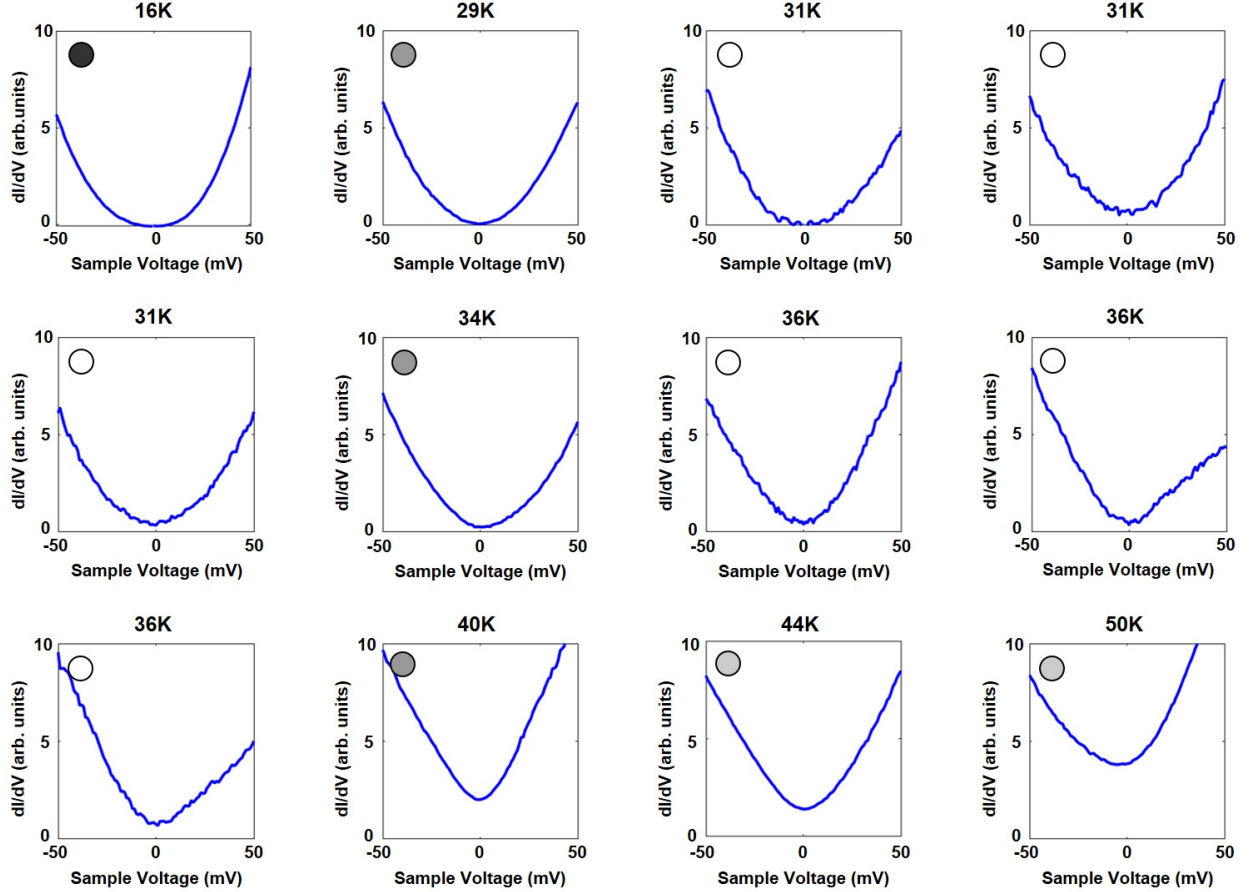


FIG. 12: STS spectra recorded at different temperatures. Selected $dI/dV(V)$ curves ordered with increasing T as marked on top. The dot in the upper left is colored identically to the extracted band gap from the same curve as displayed in Fig. 3d, main text.

D. Determination of Band Gaps at Elevated Temperature

The requirement of a more detailed analysis is demonstrated in Fig. 13a. A $dI/dV(V)$ spectrum exhibiting a gap size $\Delta = 17$ meV is displayed (blue line) as recorded at 4.3 K. This spectrum is then convolved with the derivative of the Fermi-Dirac distribution function, proportional to $1/\cosh^2(eV/2k_B T)$ [68] (other colored lines in Fig. 13a). By this convolution, we mimic the expected appearance of the same spectrum at elevated T . Obviously, the previously introduced method of gap determination would obtain $\Delta = 0$ meV for all $T \geq 31$ K, albeit the LDOS of the sample still exhibits $\Delta = 17$ meV.

In order to deduce the correct Δ from $dI/dV(V)$ curves recorded at such large T , we introduce the ratio $R = [dI/dV(0 \text{ mV})]/[dI/dV(-50 \text{ mV})]$ that turns out to be monotonously

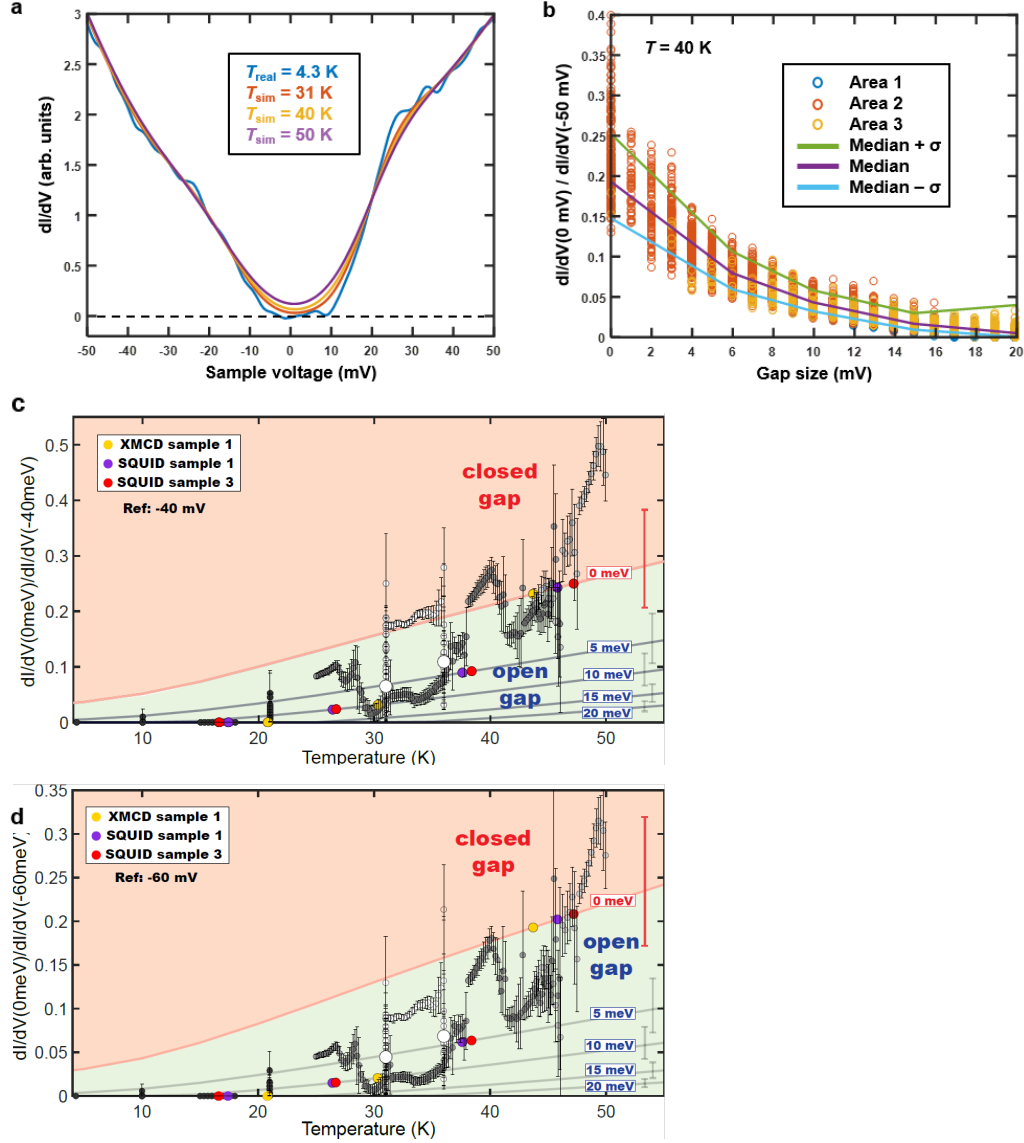


FIG. 13: **Gap size determination at elevated T .** (a) $dI/dV(V)$ spectrum with gap $\Delta = 17 \text{ meV}$ recorded at 4.3 K (blue) and the same spectrum after convolution with the derivative of the Fermi-Dirac distribution function for $T = 31 \text{ K}$ (red), $T = 40 \text{ K}$ (yellow) and $T = 50 \text{ K}$ (violet). The Fermi level broadening leads to an apparently ungapped dI/dV curve, albeit the sample LDOS features a gap of 17 meV. (b) Relation between the measured gap size Δ of $dI/dV(V)$ curves recorded at 4.3 K and the ratio $R = [dI/dV(V = 0 \text{ mV})]/[dI/dV(V = -50 \text{ mV})]$ of the same $dI/dV(V)$ curves deduced after convolution with the derivative of the Fermi-Dirac distribution function at 40 K. Different circle colors: different areas (Fig. 11). Colored lines: median (violet) surrounded by the standard deviation $\pm \sigma$ (green, blue). (c,d) Same as Fig. 3d, main text, but using a different reference voltage V_{ref} to determine R . (c) $V_{\text{ref}} = 40 \text{ mV}$, (d) $V_{\text{ref}} = 60 \text{ mV}$.

anticorrelated with the gap size Δ . This is demonstrated in Fig. 13b for $T = 40$ K. All $dI/dV(V)$ curves recorded at 4.3 K (area 1–3, 8000 curves) are convoluted with the derivative of the Fermi-Dirac distribution of 40 K (as in Fig. 13a, yellow curve) before R is determined. Subsequently, each R is related to its corresponding Δ (same $dI/dV(V)$ curve) as deduced via the method described in subsection IX B. The anticorrelation of R and Δ appears in Fig. 13b and is similarly found for all $T = 25 - 50$ K (not shown). We used the resulting median of the simulated R values (violet line in Fig. 13b) to deduce Δ from a measured R for each $dI/dV(V)$ curve recorded at elevated T . The required simulated $R(T)$ curves for constant Δ are displayed as full lines in Fig. 3d, main text, for the sake of comparison with the R values of the measured dI/dV curves. The error of $R(\Delta)$ at given T is taken as the 2σ width of the simulated $R(\Delta)$, marked by colored lines in Fig. 13b. For gap sizes below 10 meV, one observes an error of 2–4 meV only. Overall, the $R(\Delta)$ relation reaches a relative accuracy for Δ determination of $\pm 30\%$, as long as Δ remains below 20 meV. This error is displayed exemplarily on the very right of Fig. 3d, main text.

In addition, we determined errors for the measured R values. They are deduced as the standard deviation of subsequently recorded 25 $dI/dV(V)$ data sets (averaged from 10 subsequent dI/dV curves each and smoothed by box averaging of width 3 mV). The measurement errors are displayed as error bars at the data points in Fig. 3d, main text (circles). Interestingly, these measurement errors increase significantly around $T \simeq 45$ K, i.e., close to T_C , where they get as large as 10 meV. Since the spatial drift during recording of the 25 data sets is below 1 nm, as deduced by comparing the long term development of dI/dV data during cooling to the spatial fluctuations recorded at 4.3 K, these relatively large errors cannot be caused by a lateral drift of the tip with respect to the sample only. Likely, they are caused by enhanced temporal fluctuations of the gap close to T_C during recording of the 25 data sets. Thus, the increased error bars around T_C corroborate the relation of the band gap evolution to the magnetic properties additionally.

Error bars of the spatially averaged data points in Fig. 3d, main text, indicate the width of the R histograms obtained at the corresponding T .

The reference voltage $V_{\text{ref}} = -50$ mV used to determine R is chosen such that it is not influenced by temperature ($|eV_{\text{ref}}| \gg 5k_B T$) or gap size ($|eV_{\text{ref}}| \gg \max(\Delta)/2$) and not influenced by spectroscopic features that might spatially vary due to disorder. We cross-checked that the exact value of V_{ref} barely influences the deduced Δ . This is demonstrated

in Fig. 13c–d displaying the same data set as Fig. 3d, main text, but using two different V_{ref} .

X. ELECTRIC TRANSPORT MEASUREMENTS

Transport measurements were performed in the van der Pauw geometry with applied magnetic fields ranging from -3 T to +3 T and oriented parallel to the rhombohedral axis of the epilayers. A mini cryogen-free system was employed for the magnetotransport investigations at temperatures between 2 K and 300 K. For temperatures below about 50 K an anomalous Hall effect appears in the transport data that becomes hysteretic for magnetic fields of less than about 1 T such as the sheet resistance of the samples (compare Fig. 1e, main text). The carrier concentrations were determined from the Hall resistance at sufficiently high magnetic fields, i.e., well above 1 T where the sample magnetization was largely saturated. The resulting hole concentrations of the MnSb_2Te_4 samples range from $(1 - 3) \cdot 10^{20} \text{cm}^{-3}$, similar to values from the literature [30, 31].

XI. DENSITY FUNCTIONAL THEORY CALCULATIONS

A. Details of the Calculations

The electronic and magnetic structures were calculated by two different methods based on density functional theory (DFT). Most of the bulk-type calculations (Figs. 4f–k, main text, Fig. 14, Fig. 15a,b) used a Green function method within the multiple scattering theory [76, 77]. To describe both localization and interaction of the Mn $3d$ orbitals appropriately, Coulomb U values of 3–5 eV were employed within a GGA+ U approach [78]. During these calculations, we confirmed that different topological phases of MnSb_2Te_4 arise, if one uses either GGA+ U or LDA+ U , indicating that LDA+ U is not sufficient. To account for antiferromagnetic configurations of MnSb_2Te_4 , a double unit cell consisting of two septuple layers was used such as for Fig. 4k, main text, and Fig. 14a and c. In these structures, the Mn atoms couple ferromagnetically within the Mn planes and antiferromagnetically between neighboring Mn layers in adjacent septuple layers. For the determination of T_{N} and T_{C} , exchange constants J_{ij} were obtained by mapping the DFT calculations onto a classical Heisenberg model [79].

Different types of disorder were treated within a coherent potential approximation (CPA) [80, 81]. Chemical disorder is modelled by mixing various atomic species on the same atomic site (substitutional alloys). The elemental unit cell was used in this case such that only ferromagnetic order could be described. We simulated three types of chemical disorder, namely site exchange, i.e., placing as much Mn on Sb sites as Sb on Mn sites, Sb excess, i.e., additional, substitutional Sb in the Mn layers, and Mn excess, i.e., additional, substitutional Mn in the Sb layers. Electron (hole) doping was also modeled by CPA via mixing Te (Sb) vacancies, that were simulated as empty spheres, with Te (Sb) atoms on the same site. Magnetic moment disorder was modeled by CPA via mixing two Mn atoms with opposite magnetic moment on the same atomic site. This approach has been proven to be very successful in mimicking spin moment fluctuations, e.g., to account for elevated temperatures. The 50 : 50 mixing represents the paramagnetic state, while smaller spin fluctuations are described by, e.g., 95 : 5 or 98 : 2 mixings.

The calculations in Fig. 15c–f were performed with the full-potential linearized augmented plane-wave method as implemented in the FLEUR code. Also here, GGA [82] with a Hubbard U correction using $U = 6$ eV and $J = 0.54$ eV was used and spin-orbit coupling was included self-consistently in the non-collinear calculations [83]. Thin film calculations were also performed with the FLEUR code (Fig. 4c, main text, and Fig. 16b–e). These calculations are restricted to relatively small and simple unit cells in order to retain high enough accuracy to derive the Dirac cone dispersion and the size of its magnetic gap by DFT. Instead, the surface band structure for the antiferromagnetic ground state in Fig. 4d–e, main text, for the ferromagnetic ground state in Fig. 4b, main text, and for the mixed state in Fig. 16a was calculated by the projector augmented-wave method [84] using the VASP code [85, 86]. The exchange-correlation energy was treated using the GGA [82]. The Hamiltonian contained scalar relativistic corrections and the spin-orbit coupling was taken into account by the second variation method [87]. In order to describe the van der Waals interactions, we made use of the DFT-D3 [88, 89] approach. The Mn $3d$ states were treated employing the GGA+ U approximation [78] within the Dudarev scheme [90]. The $U_{\text{eff}} = U - J$ value for the Mn $3d$ states was chosen to 5.34 eV as in previous works [27, 28, 32, 56].

For all three methods, the crystal structure of ideal MnSb_2Te_4 was fully optimized to obtain the equilibrium lattice parameters, namely cell volume, c/a ratio as well as atomic positions. Using this structure yields the antiferromagnetic topological insulator state for

MnSb₂Te₄ within both the projector augmented-wave and full-potential linearized augmented plane-wave methods (VASP and FLEUR, respectively). For the Green function method both the experimental crystal structure as determined by XRD (Fig. 6) and the theoretically optimized one result in the antiferromagnetic topological insulator phase.

In order to visualize the topological character within bulk-type band structure calculations, we analyze the spectral function difference between anion and cation contributions of each state: $A_k^i(E) = A_k^{\text{anion}}(E) - A_k^{\text{cation}}(E)$. The resulting $A_k^i(E)$ are displayed as color code in Fig. 4f–k, main text, Fig. 14, and Fig. 15a,b with red color for $A_k^i(E) > 0$ and blue color for $A_k^i(E) < 0$. Band inversion can, hence, be deduced from a mutually changing color within adjacent bands.

B. Magnetic Ground State for Different Disorder Configurations

Table III summarizes the magnetic properties for four different crystallographic configurations as obtained by bulk-type DFT calculations. The ideal MnSb₂Te₄ septuple layer configuration is antiferromagnetic with low $T_N = 18$ K (third row). To probe the role of the lattice constant for the magnetic properties, we slightly expanded the lattice within the planes towards the lattice constant of MnBi₂Te₄ (last row). This led to a reduced nearest neighbor exchange constant J , but barely to a change in T_N . Introducing 5% Mn-Sb site exchange, in line with the XRD and STM data, turned the interlayer coupling ferromagnetic, but still with a $T_C = 25$ K only, i.e., significantly lower than the experimental value (fourth row). However, exchanging 2.5% of the Sb within the Sb layers by Mn without changing the Mn layers revealed $T_C = 44$ K, very close to the experimental value (fifth row). Hence, we conclude, in line with RBS, STM and XRD data, that an excess Mn in combination with an Sb deficiency is responsible for the ferromagnetic behaviour of MnSb₂Te₄ with high T_C via Mn substitution in the Sb layers.

C. Topological Properties for Different Disorder Configurations

Figure 14 shows bulk band structure calculations for antiferromagnetic MnSb₂Te₄ with ideal stoichiometric order (a,c), ideal, ferromagnetic MnSb₂Te₄ (e) and ferromagnetic MnSb₂Te₄ with increasing Mn-Sb site exchange (b,d,f). Antiferromagnetic MnSb₂Te₄ is

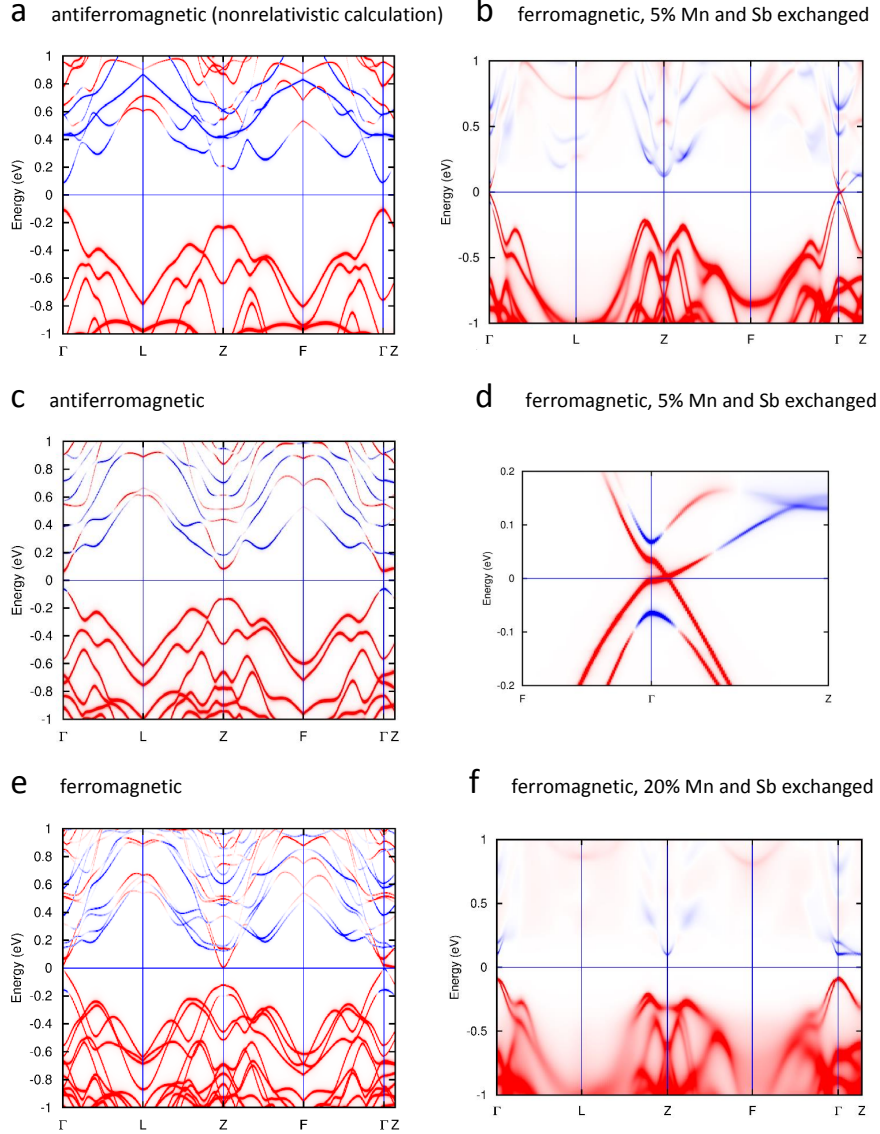


FIG. 14: **Band Structure at Different Strength of Mn-Sb Site Exchange (DFT)**. Color represents the difference between anionic and cationic spectral function for each state, red: more anionic, blue: more cationic. (a) Antiferromagnetic, ideal MnSb_2Te_4 in a nonrelativistic (more precisely scalar relativistic) calculation. No band inversion occurs. (c) Antiferromagnetic, ideal MnSb_2Te_4 in a fully relativistic calculation yielding a band inversion. Only one inversion appears in the Brillouin zone (at Γ) evidencing a Z_2 topological insulator (also shown as Fig. 4k, main text, for the ferromagnetic unit cell). (e) Same as (c) but for ferromagnetically ordered, ideal MnSb_2Te_4 with perfect out-of-plane alignment of Mn moments. A 3D Weyl semimetal occurs. The calculation used the antiferromagnetic unit cell for better comparison with (c). (b, d, f) Ferromagnetic MnSb_2Te_4 with different Mn-Sb site exchange as labeled (ferromagnetic unit cell). In (b) and (d), the Weyl point is preserved, while (f) shows a topologically trivial band gap.

direction	MnSb ₂ Te ₄				MnSb ₂ Te ₄ with lattice constants of MnBi ₂ Te ₄	
	0% disorder		5% disorder	5% extra Mn		
	T _N =18 K		T _C =25 K	T _C =44 K	T _N =20 K	
	r (Å)	J (meV)	J (meV)	J (meV)	r (Å)	J (meV)
	4.23	0.519	0.458	0.674	4.34	0.180
	7.36	-0.024	0.034	0.024	7.51	-0.007
	8.52	0.016	0.025	0.033	8.68	0.025
⊥	16.8	-0.02	0.002	0.04	16.4	-0.035

TABLE III: **Magnetic structure, critical temperature, and Mn exchange integrals of MnSb₂Te₄ for four different crystal configurations (DFT).** The exchange integrals J for the four smallest distances r between the contributing Mn ions are additionally marked by || (\perp) for intralayer (interlayer) Mn pairs. The model with 0% disorder refers to ideal MnSb₂Te₄ with all Mn atoms in the central plane of the septuple layers at the experimental lattice constants $a = 4.23$ Å, $c = 40.98$ Å (XRD). In the second model (5% disorder), a Mn-Sb site exchange leads to an occupancy of 95% Mn and 5% Sb in the central lattice plane and 2.5% Mn and 97.5% Sb in each of the two outer cationic lattice planes of the septuple layer. In the third case, 2.5% extra Mn was substitutionally introduced in the Sb layers, such that the outer cationic planes contain 2.5% Mn and 97.5% Sb, while a 100% Mn occupancy appears in the central layer. The fourth model features ideal MnSb₂Te₄ with 0% disorder, but laterally expanded to the lattice constants of MnBi₂Te₄, i.e., $a = 4.34$ Å, $c = 40.89$ Å.

a topological insulator with inverted band gap at Γ , if spin-orbit coupling is considered (c). This is contrary to previous calculations that have suggested antiferromagnetic MnSb₂Te₄ to be trivial [51–54]. We assume that the topological insulator state of antiferromagnetic MnSb₂Te₄ was missed because structural optimization was either not performed in favor of experimental lattice constants [52, 54] or performed without van der Waals forces [51, 53] which both gave by $\sim 3\%$ larger c parameters than in the structurally optimized equilibrium lattice. Ferromagnetic MnSb₂Te₄ instead, is a Weyl semimetal without band gap that remains a Weyl semimetal for moderate Mn-Sb site exchange (Fig. 14b,d), but becomes topologically trivial at large site exchange (Fig. 14f). Hence, site exchange alone does not reveal the experimentally observed ferromagnetic topological insulator in contrast to the

magnetic disorder as presented in Fig. 4g–j, main text.

Figure 15 corroborates the gap opening by magnetic disorder. Figure 15b displays the complete band structure at maximum spin mixture (50 % spin-up, 50 % spin down) for each Mn lattice site as partially presented in Fig. 4j, main text. An inverted band gap of about 100 meV is found at Γ . Note that the purely ferromagnetic phase in Fig. 15a is calculated for a unit cell of a single septuple layer only and, hence, differs from Fig. 14e employing a unit cell with two septuple layers, due to backfolding.

The Weyl point observed for the ferromagnetic MnSb_2Te_4 can also be opened by rotating the spins of adjacent Mn layers, while keeping a collinear spin order within each layer (Fig. 15c–f). Thus, magnetic disorder renders a dominantly ferromagnetic MnSb_2Te_4 a topological insulator as already discussed for Fig. 4g–j, main text.

Figure 16 shows the band structures of slab calculations for different magnetic disorder configurations, such that surface states are captured. They are performed, e.g., for a combination of ferromagnetic interior layers surrounded by a few antiferromagnetic layers on top and bottom (Fig. 16a). This configuration reveals a Dirac-type surface state with a gap around the Dirac point of 16 meV, very close to the average gap size observed by STS. The opposite configuration with antiferromagnetic interior surrounded by ferromagnetic surfaces also exhibits a gapped Dirac cone, here with 40 meV gap size, that might be enhanced by the thickness of this slab of only 7 septuple layers (Fig. 16d). Indeed, the spin-polarized states at the gap edge penetrate about 3 septuple layers into the bulk of the thin film (Fig. 16b). The out-of-plane spin polarization near the Dirac point amounts to $\sim 60\%$, nicely matching the experimentally found out-of-plane spin polarization in spin-resolved ARPES (Fig. 2j, main text). The latter amounts to $\sim 25\%$ at 30 K in line with the reduced magnetization at this elevated T (Fig. 1d,f, main text). Note that the band structure in Fig. 16d also features an exchange splitting of bulk bands as visible by the different colors around -0.2 eV.

The pure antiferromagnetic configuration (Fig. 16e) shows a small band gap of the topological surface state as well, while the pure ferromagnetic order leads to a gapped Weyl cone (Fig. 16c), likely being an artifact of the finite slab size of 7 septuple layers only.

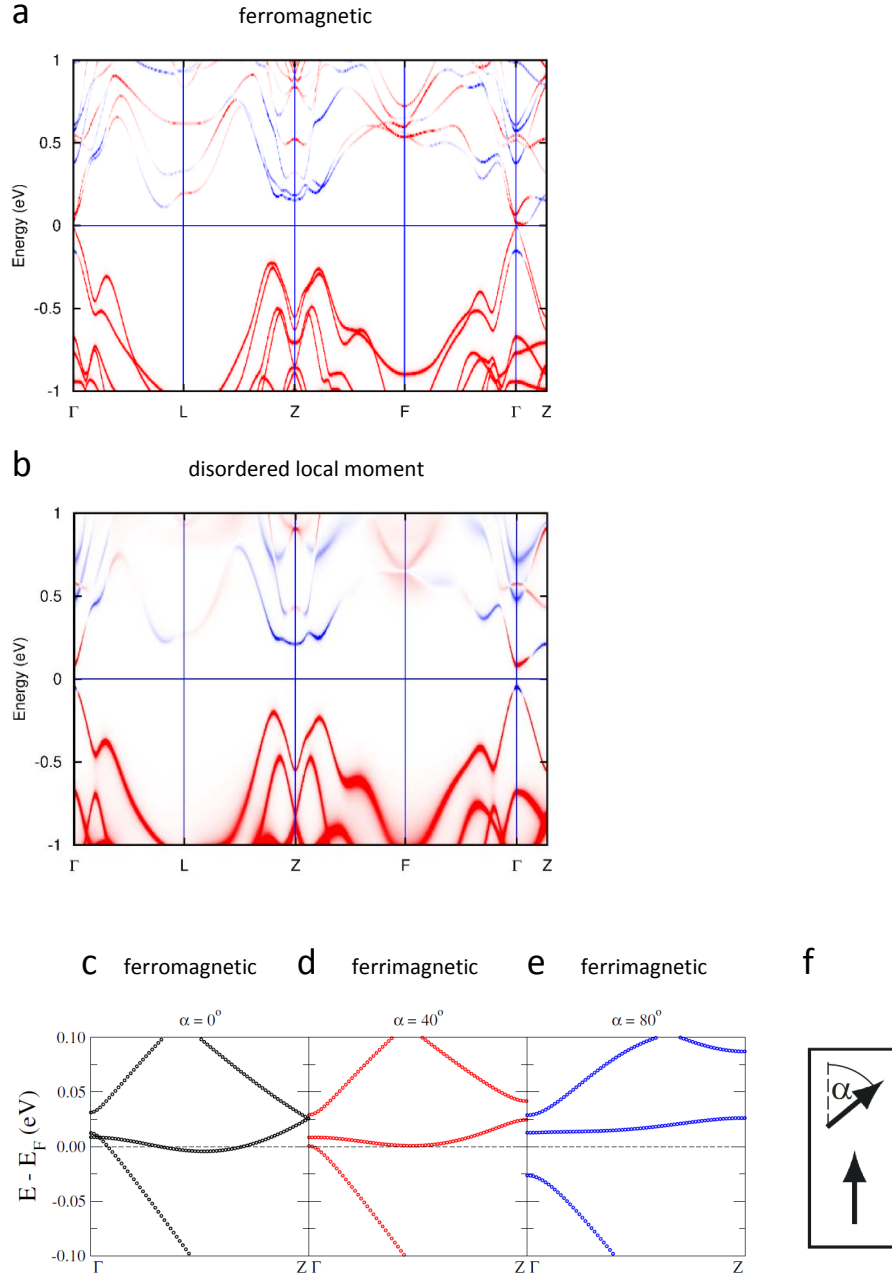


FIG. 15: **Inverted band gap by magnetic disorder (DFT).** (a) Bulk band structure of ideal, ferromagnetic MnSb_2Te_4 with Mn moments perpendicular to the septuple layers (single layer unit cell). (Part of this figure is shown as Fig. 4f, main text.) (b) Same as (a), but with disordered local magnetic moments (50% spin up, 50% spin down). An inverted band gap appears at Γ . (Part of this figure is shown as Fig. 4j, main text.) (c–e) Alternative demonstration of gap opening at the Weyl point (two septuple layer unit cell): one layer exhibits a collinear out-of-plane ferromagnetic order, while the other is also collinear, but canted relative to the first one by an angle α as marked. (f) Vector model of the collinearly canted two septuple layers.

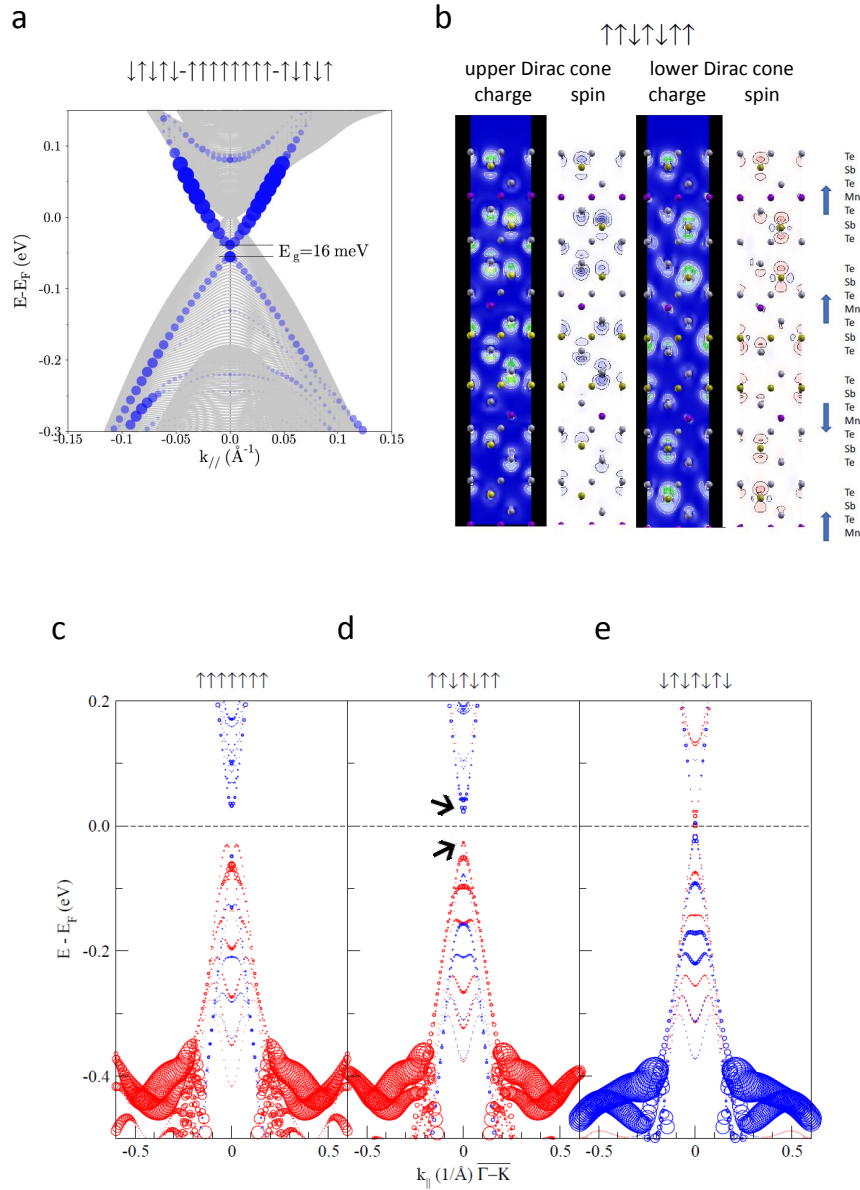


FIG. 16: Influence of magnetic structure on topological surface states (DFT). (a) Band structure for a ferromagnetic bulk surrounded by antiferromagnetic surface layers as marked on top. Blue dots are surface states with dot diameter marking their strength at the surface septuple layer. A gap appears in the topological surface state. (b) Charge density and spin density of the states at the edges of the magnetically induced band gap in (d) displayed as thin film cross section. The magnetic configuration is marked on top. (c–e) Band structure for various magnetic configurations each marked on top. Colors denote the spin density in the out-of-plane direction. (c) Ferromagnetic order with out-of-plane anisotropy. (d) Two ferromagnetic septuple layers on both sides of three antiferromagnetic layers. Black arrows mark the states shown in (b). (e) Perfect antiferromagnetic order as in Fig. 4d,e, main text.

D. Influence of Charge Doping on the Magnetic Interactions

Finally, the influence of charge doping on the magnetic properties of MnSb_2Te_4 was studied. For undoped, ideally stacked MnSb_2Te_4 , the leading magnetic interaction between the septuple layers is of a superexchange type, which is responsible for the antiferromagnetic interlayer coupling. As shown above, chemical disorder by exchanging (replacing) Mn with (by) Sb changes the magnetic order to ferromagnetic. The presence of Mn defects could induce an additional Ruderman-Kittel-Kasuya-Yoshida (RKKY) interaction that might influence the magnetic order, if mobile charges are present. However, our calculations show only minor changes of exchange constants and the magnetic transition temperatures upon charge doping. For n-type doping by 0.2% Te vacancies, E_F shifts by 0.29 eV increasing T_C by 0.9 K only. For p-type doping by 0.2% Sb vacancies, E_F shifts by -0.08 eV increasing T_C by 1.6 K. This indicates that the RKKY interaction is negligible in MnSb_2Te_4 .

-
- [1] M. Onoda, N. Nagaosa, *Phys. Rev. Lett.* **2003**, *90*, 20 206601.
 - [2] C.-X. Liu, X.-L. Qi, X. Dai, Z. Fang, S.-C. Zhang, *Phys. Rev. Lett.* **2008**, *101*, 14 146802.
 - [3] R. Yu, W. Zhang, H.-J. Zhang, S.-C. Zhang, X. Dai, Z. Fang, *Science* **2010**, *329*, 5987 61.
 - [4] Z. Qiao, S. A. Yang, W. Feng, W.-K. Tse, J. Ding, Y. Yao, J. Wang, Q. Niu, *Phys. Rev. B* **2010**, *82*, 16 161414.
 - [5] Y. Tokura, K. Yasuda, A. Tsukazaki, *Nat. Rev. Phys.* **2019**, *1*, 2 126.
 - [6] C.-Z. Chang, J. Zhang, X. Feng, J. Shen, Z. Zhang, M. Guo, K. Li, Y. Ou, P. Wei, L.-L. Wang, Z.-Q. Ji, Y. Feng, S. Ji, X. Chen, J. Jia, X. Dai, Z. Fang, S.-C. Zhang, K. He, Y. Wang, L. Lu, X.-C. Ma, Q.-K. Xue, *Science* **2013**, *340*, 6129 167.
 - [7] J. G. Checkelsky, R. Yoshimi, A. Tsukazaki, K. S. Takahashi, Y. Kozuka, J. Falson, M. Kawasaki, Y. Tokura, *Nat. Phys.* **2014**, *10*, 10 731.
 - [8] X. Kou, S.-T. Guo, Y. Fan, L. Pan, M. Lang, Y. Jiang, Q. Shao, T. Nie, K. Murata, J. Tang, Y. Wang, L. He, T.-K. Lee, W.-L. Lee, K. L. Wang, *Phys. Rev. Lett.* **2014**, *113*, 13 137201.
 - [9] A. Bestwick, E. Fox, X. Kou, L. Pan, K. L. Wang, D. Goldhaber-Gordon, *Phys. Rev. Lett.* **2015**, *114*, 18 187201.
 - [10] A. Kandala, A. Richardella, S. Kempinger, C.-X. Liu, N. Samarth, *Nat. Commun.* **2015**, *6*,

1 7434.

- [11] C.-Z. Chang, W. Zhao, D. Y. Kim, H. Zhang, B. A. Assaf, D. Heiman, S.-C. Zhang, C. Liu, M. H. W. Chan, J. S. Moodera, *Nat. Mater.* **2015**, *14*, 5 473.
- [12] S. Grauer, S. Schreyeck, M. Winnerlein, K. Brunner, C. Gould, L. W. Molenkamp, *Phys. Rev. B* **2015**, *92*, 20 201304.
- [13] E. J. Fox, I. T. Rosen, Y. Yang, G. R. Jones, R. E. Elmquist, X. Kou, L. Pan, K. L. Wang, D. Goldhaber-Gordon, *Phys. Rev. B* **2018**, *98*, 7 075145.
- [14] M. Götz, K. M. Fijalkowski, E. Pesel, M. Hartl, S. Schreyeck, M. Winnerlein, S. Grauer, H. Scherer, K. Brunner, C. Gould, F. J. Ahlers, L. W. Molenkamp, *Appl. Phys. Lett.* **2018**, *112*, 7 072102.
- [15] M. Ye, W. Li, S. Zhu, Y. Takeda, Y. Saitoh, J. Wang, H. Pan, M. Nurmamat, K. Sumida, F. Ji, Z. Liu, H. Yang, Z. Liu, D. Shen, A. Kimura, S. Qiao, X. Xie, *Nat. Commun.* **2015**, *6*, 1 8913.
- [16] M. Li, C.-Z. Chang, L. Wu, J. Tao, W. Zhao, M. H. Chan, J. S. Moodera, J. Li, Y. Zhu, *Phys. Rev. Lett.* **2015**, *114*, 14 146802.
- [17] M. Mogi, R. Yoshimi, A. Tsukazaki, K. Yasuda, Y. Kozuka, K. S. Takahashi, M. Kawasaki, Y. Tokura, *Appl. Phys. Lett.* **2015**, *107*, 18 182401.
- [18] H. Deng, Z. Chen, A. Wołoś, M. Konczykowski, K. Sobczak, J. Sitnicka, I. V. Fedorchenko, J. Borysiuk, T. Heider, L. Pluciński, K. Park, A. B. Georgescu, J. Cano, L. Krusin-Elbaum, *Nat. Phys.* **2020**, *17*, 1 36.
- [19] Z. Zhou, Y.-J. Chien, C. Uher, *Appl. Phys. Lett.* **2005**, *87*, 11 112503.
- [20] X. Zhang, S.-C. Zhang, In T. George, M. S. Islam, A. Dutta, editors, *Micro- and Nanotechnology Sensors, Systems, and Applications IV*. SPIE, **2012** URL <https://doi.org/10.1117/12.920325>.
- [21] K. Yasuda, M. Mogi, R. Yoshimi, A. Tsukazaki, K. S. Takahashi, M. Kawasaki, F. Kagawa, Y. Tokura, *Science* **2017**, *358*, 6368 1311.
- [22] A. C. Mahoney, J. I. Colless, L. Peeters, S. J. Pauka, E. J. Fox, X. Kou, L. Pan, K. L. Wang, D. Goldhaber-Gordon, D. J. Reilly, *Nat. Commun.* **2017**, *8*, 1 1836.
- [23] D. Xiao, J. Jiang, J.-H. Shin, W. Wang, F. Wang, Y.-F. Zhao, C. Liu, W. Wu, M. H. Chan, N. Samarth, C.-Z. Chang, *Phys. Rev. Lett.* **2018**, *120*, 5 056801.
- [24] E. D. L. Rienks, S. Wimmer, J. Sánchez-Barriga, O. Caha, P. S. Mandal, J. Růžicka, A. Ney,

- H. Steiner, V. V. Volobuev, H. Groiss, M. Albu, G. Kothleitner, J. Michalička, S. A. Khan, J. Minár, H. Ebert, G. Bauer, F. Freyse, A. Varykhalov, O. Rader, G. Springholz, *Nature* **2019**, *576*, 7787 423.
- [25] J. A. Hagmann, X. Li, S. Chowdhury, S.-N. Dong, S. Rouvimov, S. J. Pookpanratana, K. M. Yu, T. A. Orlova, T. B. Bolin, C. U. Segre, D. G. Seiler, C. A. Richter, X. Liu, M. Dobrowolska, J. K. Furdyna, *New J. Phys.* **2017**, *19*, 8 085002.
- [26] D. S. Lee, T.-H. Kim, C.-H. Park, C.-Y. Chung, Y. S. Lim, W.-S. Seo, H.-H. Park, *Cryst. Eng. Comm* **2013**, *15*, 27 5532.
- [27] S. Eremeev, M. Otrokov, E. Chulkov, *J. Alloys Compd.* **2017**, *709* 172.
- [28] M. M. Otrokov, I. I. Klimovskikh, H. Bentmann, D. Estyunin, A. Zeugner, Z. S. Aliev, S. Gaß, A. U. B. Wolter, A. V. Koroleva, A. M. Shikin, M. Blanco-Rey, M. Hoffmann, I. P. Rusinov, A. Y. Vyazovskaya, S. V. Eremeev, Y. M. Koroteev, V. M. Kuznetsov, F. Freyse, J. Sánchez-Barriga, I. R. Amiraslanov, M. B. Babanly, N. T. Mamedov, N. A. Abdullayev, V. N. Zverev, A. Alfonsov, V. Kataev, B. Büchner, E. F. Schwier, S. Kumar, A. Kimura, L. Petaccia, G. D. Santo, R. C. Vidal, S. Schatz, K. Kißner, M. Ünzelmann, C. H. Min, S. Moser, T. R. F. Peixoto, F. Reinert, A. Ernst, P. M. Echenique, A. Isaeva, E. V. Chulkov, *Nature* **2019**, *576*, 7787 416.
- [29] J.-Q. Yan, Q. Zhang, T. Heitmann, Z. Huang, K. Y. Chen, J.-G. Cheng, W. Wu, D. Vaknin, B. C. Sales, R. J. McQueeney, *Phys. Rev. Mat.* **2019**, *3*, 6 064202.
- [30] J.-Q. Yan, S. Okamoto, M. A. McGuire, A. F. May, R. J. McQueeney, B. C. Sales, *Phys. Rev. B* **2019**, *100*, 10 104409.
- [31] Y. Chen, Y.-W. Chuang, S. H. Lee, Y. Zhu, K. Honz, Y. Guan, Y. Wang, K. Wang, Z. Mao, J. Zhu, C. Heikes, P. Quarterman, P. Zajdel, J. A. Borchers, W. Ratcliff, *Phys. Rev. Mat.* **2020**, *4*, 6 064411.
- [32] M. Otrokov, I. Rusinov, M. Blanco-Rey, M. Hoffmann, A. Vyazovskaya, S. Eremeev, A. Ernst, P. Echenique, A. Arnau, E. Chulkov, *Phys. Rev. Lett.* **2019**, *122*, 10 107202.
- [33] Y.-J. Hao, P. Liu, Y. Feng, X.-M. Ma, E. F. Schwier, M. Arita, S. Kumar, C. Hu, R. Lu, M. Zeng, Y. Wang, Z. Hao, H.-Y. Sun, K. Zhang, J. Mei, N. Ni, L. Wu, K. Shimada, C. Chen, Q. Liu, C. Liu, *Phys. Rev. X* **2019**, *9*, 4 041038.
- [34] H. Li, S.-Y. Gao, S.-F. Duan, Y.-F. Xu, K.-J. Zhu, S.-J. Tian, J.-C. Gao, W.-H. Fan, Z.-C. Rao, J.-R. Huang, J.-J. Li, D.-Y. Yan, Z.-T. Liu, W.-L. Liu, Y.-B. Huang, Y.-L. Li, Y. Liu,

- G.-B. Zhang, P. Zhang, T. Kondo, S. Shin, H.-C. Lei, Y.-G. Shi, W.-T. Zhang, H.-M. Weng, T. Qian, H. Ding, *Phys. Rev. X* **2019**, *9*, 4 041039.
- [35] Y. J. Chen, L. X. Xu, J. H. Li, Y. W. Li, H. Y. Wang, C. F. Zhang, H. Li, Y. Wu, A. J. Liang, C. Chen, S. W. Jung, C. Cacho, Y. H. Mao, S. Liu, M. X. Wang, Y. F. Guo, Y. Xu, Z. K. Liu, L. X. Yang, Y. L. Chen, *Phys. Rev. X* **2019**, *9*, 4 041040.
- [36] Y. Deng, Y. Yu, M. Z. Shi, Z. Guo, Z. Xu, J. Wang, X. H. Chen, Y. Zhang, *Science* **2020**, *367*, 6480 895.
- [37] R. C. Vidal, A. Zeugner, J. I. Facio, R. Ray, M. H. Haghighi, A. U. Wolter, L. T. C. Bohorquez, F. Caglieris, S. Moser, T. Figgemeier, T. R. Peixoto, H. B. Vasili, M. Valvidares, S. Jung, C. Cacho, A. Alfonsov, K. Mehlawat, V. Kataev, C. Hess, M. Richter, B. Büchner, J. van den Brink, M. Ruck, F. Reinert, H. Bentmann, A. Isaeva, *Phys. Rev. X* **2019**, *9*, 4 041065.
- [38] C. Hu, L. Ding, K. N. Gordon, B. Ghosh, H.-J. Tien, H. Li, A. G. Linn, S.-W. Lien, C.-Y. Huang, S. Mackey, J. Liu, P. V. S. Reddy, B. Singh, A. Agarwal, A. Bansil, M. Song, D. Li, S.-Y. Xu, H. Lin, H. Cao, T.-R. Chang, D. Dessau, N. Ni, *Sci. Adv.* **2020**, *6*, 30 eaba4275.
- [39] B. Chen, F. Fei, D. Wang, Z. Jiang, B. Zhang, J. Guo, H. Xie, Y. Zhang, M. Naveed, Y. Du, Z. Sun, H. Zhang, D. Shen, F. Song, *arXiv* **2020**, *2009*. 00039.
- [40] G. Shi, M. Zhang, D. Yan, H. Feng, M. Yang, Y. Shi, Y. Li, *Chin. Phys. Lett.* **2020**, *37*, 4 047301.
- [41] C. Hu, S. Mackey, N. Ni, *arXiv* **2020**, *2008*. 09097.
- [42] S. Huan, S. Zhang, Z. Jiang, H. Su, H. Wang, X. Zhang, Y. Yang, Z. Liu, X. Wang, N. Yu, Z. Zou, D. Shen, J. Liu, Y. Guo, *arXiv* **2021**, *2101*. 10149.
- [43] C. Pauly, G. Bihlmayer, M. Liebmann, M. Grob, A. Georgi, D. Subramaniam, M. R. Scholz, J. Sánchez-Barriga, A. Varykhalov, S. Blügel, O. Rader, M. Morgenstern, *Phys. Rev. B* **2012**, *86*, 23 235106.
- [44] J. S. Dyck, P. Svanda, P. Lostak, J. Horak, W. Chen, C. Uher, *J. Appl. Phys.* **2003**, *94*, 12 7631.
- [45] J. Choi, S. Choi, J. Choi, Y. Park, H.-M. Park, H.-W. Lee, B.-C. Woo, S. Cho, *phys. stat. sol. (b)* **2004**, *241*, 7 1541.
- [46] Y. Liu, L.-L. Wang, Q. Zheng, Z. Huang, X. Wang, M. Chi, Y. Wu, B. C. Chakoumakos, M. A. McGuire, B. C. Sales, W. Wu, J. Yan, *arXiv* **2020**, *2007*. 12217.
- [47] T. Murakami, Y. Nambu, T. Koretsune, G. Xiangyu, T. Yamamoto, C. M. Brown,

- H. Kageyama, *Phys. Rev. B* **2019**, *100*, 19 195103.
- [48] W. Ge, P. M. Sass, J. Yan, S. H. Lee, Z. Mao, W. Wu, *Phys. Rev. B* **2021**, *103* 134403.
- [49] S. X. M. Riberolles, Q. Zhang, E. Gordon, N. P. Butch, L. Ke, J. Q. Yan, R. J. McQueeney, *arXiv* **2021**, *2103*. 09335.
- [50] H. Li, Y. Li, Y.-K. Lian, W. Xie, L. Chen, J. Zhang, Y. Wu, S. Fan, *arXiv* **2021**, *2104*. 00898.
- [51] D. Zhang, M. Shi, T. Zhu, D. Xing, H. Zhang, J. Wang, *Phys. Rev. Lett.* **2019**, *122*, 20 206401.
- [52] B. Chen, F. Fei, D. Zhang, B. Zhang, W. Liu, S. Zhang, P. Wang, B. Wei, Y. Zhang, Z. Zuo, J. Guo, Q. Liu, Z. Wang, X. Wu, J. Zong, X. Xie, W. Chen, Z. Sun, S. Wang, Y. Zhang, M. Zhang, X. Wang, F. Song, H. Zhang, D. Shen, B. Wang, *Nat. Commun.* **2019**, *10*, 1 4469.
- [53] C. Lei, S. Chen, A. H. MacDonald, *Proc. Natl. Acad. Sci.* **2020**, *117*, 44 27224.
- [54] Y. Liu, L.-L. Wang, Q. Zheng, Z. Huang, X. Wang, M. Chi, Y. Wu, B. C. Chakoumakos, M. A. McGuire, B. C. Sales, W. Wu, J. Yan, *arXiv* **2020**, *2007*. 12217.
- [55] L. Zhou, Z. Tan, D. Yan, Z. Fang, Y. Shi, H. Weng, *Phys. Rev. B* **2020**, *102*, 8 085114.
- [56] M. M. Otrokov, T. V. Menshchikova, M. G. Vergniory, I. P. Rusinov, A. Y. Vyazovskaya, Y. M. Koroteev, G. Bihlmayer, A. Ernst, P. M. Echenique, A. Arnau, E. V. Chulkov, *2D Mater.* **2017**, *4*, 2 025082.
- [57] C. L. Richardson, J. M. Devine-Stoneman, G. Divitini, M. E. Vickers, C.-Z. Chang, M. Amado, J. S. Moodera, J. W. A. Robinson, *Sci. Rep.* **2017**, *7*, 1 12061.
- [58] Y. Jiang, Y. Y. Sun, M. Chen, Y. Wang, Z. Li, C. Song, K. He, L. Wang, X. Chen, Q.-K. Xue, X. Ma, S. B. Zhang, *Phys. Rev. Lett.* **2012**, *108*, 6 066809.
- [59] J. Kellner, G. Bihlmayer, V. L. Deringer, M. Liebmann, C. Pauly, A. Giussani, J. E. Boschker, R. Calarco, R. Dronskowski, M. Morgenstern, *Phys. Rev. B* **2017**, *96*, 24 245408.
- [60] Y. Yuan, X. Wang, H. Li, J. Li, Y. Ji, Z. Hao, Y. Wu, K. He, Y. Wang, Y. Xu, W. Duan, W. Li, Q.-K. Xue, *Nano Lett.* **2020**, *20*, 5 3271.
- [61] Y. Lai, L. Ke, J. Yan, R. D. McDonald, R. J. McQueeney, *arXiv* **2021**, *2102*. 05797.
- [62] J. Sánchez-Barriga, A. Varykhalov, G. Springholz, H. Steiner, R. Kirchschlager, G. Bauer, O. Caha, E. Schierle, E. Weschke, A. A. Ünal, S. Valencia, M. Dunst, J. Braun, H. Ebert, J. Minár, E. Golias, L. V. Yashina, A. Ney, V. Holý, O. Rader, *Nat. Commun.* **2016**, *7*, 1 10559.
- [63] J. Henk, M. Flieger, I. V. Maznichenko, I. Mertig, A. Ernst, S. V. Eremeev, E. V. Chulkov,

- Phys. Rev. Lett.* **2012**, *109* 076801.
- [64] I. Lee, C. K. Kim, J. Lee, S. J. L. Billinge, R. Zhong, J. A. Schneeloch, T. Liu, T. Valla, J. M. Tranquada, G. Gu, J. C. S. Davis, *Proc. Natl. Acad. Sci.* **2015**, *112*, 5 1316.
- [65] C.-C. Chen, M. L. Teague, L. He, X. Kou, M. Lang, W. Fan, N. Woodward, K.-L. Wang, N.-C. Yeh, *New J. Phys.* **2015**, *17*, 11 113042.
- [66] H. Beidenkopf, P. Roushan, J. Seo, L. Gorman, I. Drozdov, Y. S. Hor, R. J. Cava, A. Yazdani, *Nat. Phys.* **2011**, *7*, 12 939.
- [67] C. Pauly, C. Saunus, M. Liebmann, M. Morgenstern, *Phys. Rev. B* **2015**, *92*, 8 085140.
- [68] M. Morgenstern, *Surf. Rev. Lett.* **2003**, *10*, 06 933.
- [69] P. Sessi, R. R. Biswas, T. Bathon, O. Storz, S. Wilfert, A. Barla, K. A. Kokh, O. E. Tereshchenko, K. Fauth, M. Bode, A. V. Balatsky, *Nat. Commun.* **2016**, *7*, 1 12027.
- [70] G. Rosenberg, M. Franz, *Phys. Rev. B* **2012**, *85*, 19 195119.
- [71] T. R. Kirkpatrick, D. Belitz, *Phys. Rev. B* **2015**, *91*, 21 214407.
- [72] D. Fuchs, M. Wissinger, J. Schmalian, C.-L. Huang, R. Fromknecht, R. Schneider, H. v. Löhneysen, *Phys. Rev. B* **2014**, *89*, 17 174405.
- [73] B. C. Sales, K. Jin, H. Bei, J. Nichols, M. F. Chisholm, A. F. May, N. P. Butch, A. D. Christianson, M. A. McGuire, *npj Quantum Materials* **2017**, *2*, 1 33.
- [74] M. Mayer, *Nuclear Instrum. Methods B* **2014**, *332* 176.
- [75] H. Steiner, V. Volobuev, O. Caha, G. Bauer, G. Springholz, V. Holý, *J. Appl. Cryst.* **2014**, *47*, 6 1889.
- [76] B. L. Gyorffy, M. J. Stott, In D. J. Fabian, L. M. Watson, editors, *Proc. of the Int. Conf. on Band Structure and Spectroscopy of Metals and Alloys*. Academic Press, **1973** 385.
- [77] M. Geilhufe, S. Achilles, M. A. Köbis, M. Arnold, I. Mertig, W. Hergert, A. Ernst, *J. Phys.: Condens. Matter* **2015**, *27*, 43 435202.
- [78] V. I. Anisimov, J. Zaanen, O. K. Andersen, *Phys. Rev. B* **1991**, *44*, 3 943.
- [79] A. Liechtenstein, M. Katsnelson, V. Antropov, V. Gubanov, *J. Magn. Magn. Mat.* **1987**, *67*, 1 65.
- [80] P. Soven, *Phys. Rev.* **1967**, *156*, 3 809.
- [81] B. L. Gyorffy, *Phys. Rev. B* **1972**, *5*, 6 2382.
- [82] J. P. Perdew, K. Burke, M. Ernzerhof, *Phys. Rev. Lett.* **1996**, *77*, 18 3865.
- [83] P. Kurz, F. Förster, L. Nordström, G. Bihlmayer, S. Blügel, *Phys. Rev. B* **2004**, *69* 024415.

- [84] P. E. Blöchl, *Phys. Rev. B* **1994**, *50*, 24 17953.
- [85] G. Kresse, J. Furthmüller, *Phys. Rev. B* **1996**, *54*, 16 11169.
- [86] G. Kresse, D. Joubert, *Phys. Rev. B* **1999**, *59*, 3 1758.
- [87] D. D. Koelling, B. N. Harmon, *Journal of Physics C: Solid State Physics* **1977**, *10*, 16 3107.
- [88] S. Grimme, J. Antony, S. Ehrlich, H. Krieg, *J. Chem. Phys.* **2010**, *132*, 15 154104.
- [89] S. Grimme, S. Ehrlich, L. Goerigk, *J. Comput. Chem.* **2011**, *32*, 7 1456.
- [90] S. L. Dudarev, G. A. Botton, S. Y. Savrasov, C. J. Humphreys, A. P. Sutton, *Phys. Rev. B* **1998**, *57*, 3 1505.